The Astrophysical Journal, 650:573–591, 2006 October 20
© 2006. The American Astronomical Society. All rights reserved. Printed in U.S.A.

WHERE ARE THE BARYONS? III. NONEQUILIBRIUM EFFECTS AND OBSERVABLES

Renyue Cen[1] and Taotao Fang[2,3]

Received 2005 December 27; accepted 2006 April 20

ABSTRACT

A significant fraction (40%–50%) of baryons at the present epoch are predicted to be shock-heated to the warm-hot intergalactic medium (WHIM) by our previous numerical simulations. Here we recompute the evolution of the WHIM with several major improvements: (1) galactic superwind feedback processes from galaxy and star formation are explicitly included; (2) major metal species (O v to O ix) are computed explicitly in a nonequilibrium way; and (3) mass and spatial dynamic ranges are larger by factors of 8 and 2, respectively, than in our previous simulations. We find the following: (1) Nonequilibrium calculations produce significantly different results than do ionization equilibrium calculations. (2) The abundance of O vi absorption lines based on nonequilibrium simulations with galactic superwinds is in remarkably good agreement with the latest observations, strongly validating our model, while the predicted abundances for O vii and O viii absorption lines appear to be lower than the still very uncertain observations. The expected abundances for O vi (as well as Lyα), O vii, and O viii absorption systems are in the range 50–100 per unit redshift at equivalent width EW = 1 km s^{-1}, decreasing to 10–20 per unit redshift at EW = 10 km s^{-1}, to one to three lines for O vii and O viii and negligible for O vi at EW > 100 km s^{-1}. (3) Emission lines, primarily O vi and Lyα in the UV and O vii and O viii in soft X-rays, are potentially observable by future missions, and different lines provide complementary probes of the WHIM in the temperature-density-metallicity phase space. The number of emission lines per unit redshift that may be detectable by planned UV and soft X-ray missions are of order 0.1–1.

Subject headings: cosmology: observations — intergalactic medium — large-scale structure of universe

Online material: color figures

1. INTRODUCTION

Cosmological hydrodynamic simulations have strongly suggested that most of the previously "missing" baryons may be in a gaseous phase in the temperature range 10^5–10^7 K and at moderate overdensity (Cen & Ostriker 1999; Davé et al. 2001), called the warm-hot intergalactic medium (WHIM), with the primary heating process being hydrodynamic shocks from the formation of large-scale structure at scales currently becoming nonlinear. The reality of the WHIM has now been quite convincingly confirmed by a number of observations from the *Hubble Space Telescope*, the *Far Ultraviolet Spectroscopic Explorer*, *Chandra*, and *XMM-Newton* (Tripp et al. 2000; Tripp & Savage 2000; Oegerle et al. 2000; Scharf et al. 2000; Tittley & Henriksen 2001; Savage et al. 2002; Fang et al. 2002b; Nicastro et al. 2002; Mathur et al. 2003; Kaastra et al. 2003; Finoguenov et al. 2003; Sembach et al. 2004; Nicastro et al. 2005).

In addition to shock heating, feedback processes following star formation in galaxies can heat gas to the same WHIM temperature range. What is lacking theoretically is a satisfactory understanding of the known feedback processes on the WHIM and how the WHIM may be used to understand and calibrate the feedback processes. Another unsettled issue is how the predicted results will change if one has a more accurate, nonequilibrium calculation of the major metal species, such as O vi, O vii, and O viii, since the timescales for ionization and recombination are not widely separated from the Hubble timescale. In a companion paper (Cen & Ostriker 2006), we studied the effects of galactic superwinds on the intergalactic medium (IGM), and in particular on the WHIM. Additional improvements include significantly larger dynamic ranges in the simulation, a cosmological model normalized to measurements from the *Wilkinson Microwave Anistropy Probe* (*WMAP*), and an improved radiative transfer treatment. The purpose of this paper is to present additional effects due to nonequilibrium calculations on major observable metal species, such as O vi, O vii, and O viii. Our current work significantly extends previous theoretical works by our group and others (Cen & Ostriker 1999; Davé et al. 2001; Cen et al. 2001; Fang et al. 2002a; Chen et al. 2003; Furlanetto et al. 2004, 2005a, 2005b; Yoshikawa et al. 2003; Suto et al. 2004; Fang et al. 2005; Ohashi et al. 2006). The outline of this paper is as follows: the simulation details are given in § 2, in § 3 we give detailed results and discussion, and conclusions are presented in § 4.

2. SIMULATIONS

The reader should refer to Cen & Ostriker (2006) for a detailed description of the computational method. Here we will only briefly explain the basic hydrodynamic code, the cosmological model that we use, the simulation box parameters, and relevant treatment details on how major oxygen species are computed.

The results reported here are based on new simulations of a *WMAP*-normalized (Spergel et al. 2003; Tegmark et al. 2004) cold dark matter model with a cosmological constant, $\Omega_m = 0.31$, $\Omega_b = 0.048$, $\Omega_\Lambda = 0.69$, $\sigma_8 = 0.89$, $H_0 = 100\ h$ km s^{-1} Mpc^{-1} = 69 km s^{-1} Mpc^{-1}, and $n = 0.97$. The adopted box size is 85 h^{-1} Mpc comoving and with a number of cells of 1024^3; the cell size is 83 h^{-1} kpc comoving, with dark matter particle mass equal to $3.9 \times 10^8\ h^{-1}\ M_\odot$. Given a lower bound of the temperature for almost all the gas in the simulation of $T \sim 10^4$ K, the Jeans mass is $\sim 10^{10}\ M_\odot$ for mean-density gas, which is comfortably larger than our mass resolution.

As described in Cen & Ostriker (2006), we have made simulations with and without galactic superwinds. Metals are produced

---

[1] Princeton University Observatory, Peyton Hall, Princeton, NJ 08544; cen@astro.princeton.edu.

[2] Department of Astronomy, University of California, Berkeley, 601 Campbell Hall, Berkeley, CA 94720; fangt@astro.berkeley.edu.

[3] *Chandra* Fellow.

self-consistently from star formation by adopting a specific efficiency of metal formation, a "yield" (Arnett 1996) $y_0 = 0.02$, the percentage of stellar mass that is ejected back into IGM as metals for Type II supernovae (SNe II), which we follow accurately in the simulation. On the other hand, accurately following the evolution of metal ejection (approximately half the iron) from Type I supernovae (SNe I) is difficult, in large part because of the uncertainties in theoretical modeling of SNe I. Since oxygen is predominantly produced by SNe II, our results on oxygen-related quantities are very insensitive to the lack of treatment of SNe I. Metals produced by SNe II are followed as a separate variable (analogous to the total gas density) with the same hydrocode. In addition, we implement another density variable to keep track of the reprocessed, that is, secondary, metals in the ejecta (such as *s*-process elements), which are proportional to the metallicity of the gas from which the star was formed. There are two adjustable parameters with regard to overall metal production, namely, y_0 from SNe II and y_I from SNe I in terms of metal contribution. These two parameters are uncertain theoretically but may be normalized by observed oxygen and iron abundances in the intracluster medium (ICM). The oxygen and iron abundances are ~0.5 and ~0.3 times solar, respectively, in the ICM of observed clusters (e.g., Mushotzky et al. 1996; Tamura et al. 2004), and there are indications that there is about an equal contribution to the iron mass in the ICM from SNe Ia and SNe II (e.g., Ettori 2005). Following Tsujimoto et al. (1995), using metal yield patterns for SNe Ia and SNe II with a Salpeter initial mass function (IMF), we find that in order to match the observed iron metallicity of ~0.3 times solar in the ICM, we need an SNe II metal yield $y_0 = 0.03$ instead of the adopted value of 0.02, taking into account that half of the iron in the ICM would have been contributed by SNe Ia. However, this still leaves us with an oxygen abundance in the computed ICM of ~0.25 times solar (using $y_0 = 0.03$), versus the observed value of ~0.5 times solar (Mushotzky et al. 1996; Tamura et al. 2004). This deficit in oxygen mass in the ICM cannot be made up by SNe Ia in any reasonable abundance, because they do not produce a significant amount of oxygen mass. We do not yet know the actual solution to this problem. Possible solutions may include an IMF that is significantly flatter than the adopted Salpeter IMF, which would produce more SNe II and more hypernovae, which are prime producers of oxygen. Alternatively, one may increase the star formation efficiency by some factor, say, ~2, to bring the oxygen abundance into better agreement with observations, which would then require some adjustment to the contribution to iron mass in the ICM from SNe Ia. This is a very complex issue, and there may be hints that a simple combination of SNe II and SNe Ia with the standard IMF may not be adequate (e.g., Dupke & White 2000; Portinari et al. 2004; Baumgartner et al. 2005); it is beyond the scope of this paper to attempt to address this issue. What we must do, however, is to normalize the simulated abundances of both iron and oxygen to the observed values in the ICM as closely as we can. This requirement translates to an enhancement of oxygen abundance by a factor of $\sim 3 = 0.03/0.02 \times 2$, where the factor 0.03/0.02 is needed to normalize to the ICM iron abundance (see Fig. 15 below) and the factor 2 is to further normalize to the ICM oxygen abundance; we stress again that the underlying cause for the factor of 2 is unclear at present. Aside from this unknown scaling factor, oxygen is known to be predominantly produced by SNe II, and hence the computed spatial and temporal evolution of the oxygen distribution should remain accurate; we simply multiply the oxygen abundance at every spatial point in the simulation by a factor of 3. Once this renormalization procedure is done, we have no further freedom to make any other adjustment with regard to metallicity—specifically, oxygen abundances—in any other regions of the IGM, which are the focus of this study. We have adopted a solar oxygen abundance of 8.78 dex, which is close to, but about 20% higher than, recently determined values (Allende Prieto et al. 2001; Asplund et al. 2004).

The implementation of the major oxygen species is done as follows: We follow the evolution of O IV to O IX simultaneously by directly integrating five rate equations for each cell in a nonequilibrium fashion. Each oxygen species is followed as a separate variable, and each conservation equation (without the source terms) is solved using the same TVD (toal variation diminishing) hydrodynamics code, taking into account recombination (Shull & Van Steenberg 1982), collisional ionization (Aldrovandi & Péquignot 1973; Shull & Van Steenberg 1982; Arnaud & Rothenflug 1985; Arnaud & Raymond 1992; Verner & Ferland 1996; Voronov 1997), and photoionization (Clark et al. 1986; Verner et al. 1996) processes for a nonuniform cosmological density field. Relevant coefficients for these processes and equations are included in the Appendix for completeness. We note that the nonequilibrium treatment of different oxygen species does not have an impact upon the gas dynamics and observable stellar properties of galaxies.

3. RESULTS

We present and compare simulations with and without galactic superwinds (GSWs; Cen & Ostriker 2006) and between calculations that assume ionization equilibrium and detailed nonequilibrium calculations.

3.1. *Metal Absorption Lines in UV and X-Rays*

We present detailed results on major absorption lines, including O VI λλ1032, 1038, O VII λ21.6, and O VIII λ19.0. The detailed evolution of all these major metal species is followed in a nonequilibrium fashion, by solving rate equations for each cell at each time step explicitly. The evolution also depends on the detailed background radiation field as a function of redshift, which we compute in a self-consistent way in our simulations, taking into account both sources and sinks computed directly in the simulations, shown in Figure 1. All our results presented below are at $z \sim 0$, and hence the $z = 0$ radiation field is used when we compute metal abundances for some species based on the Cloudy (equilibrium) method (Ferland et al. 1998). We note that the computed $z = 0$ radiation field is consistent with observations (Shull et al. 1999), as is the radiation field at higher redshifts (Rauch et al. 1997; Bolton et al. 2005), and with the observationally derived evolution of the background radiation field (Haardt & Madau 1996). The absorption lines are identified using the same method as used by Fang et al. (2002a).

Figure 2 shows the number of O VI absorption lines per unit redshift as a function of equivalent width from simulations with and without GSWs, and from the case based on the simulation using the program Cloudy with GSWs, all compared with observations. First, we note that the simulation with appropriate GSWs and nonequilibrium calculation (*solid curve*) is in excellent agreement with direct observations (*filled circles*). This is quite remarkable, considering that we have not attempted any fine-tuning of model parameters and the only two major parameters that have significant effects are $e_{\rm GSW}$ and y, where the latter is normalized to the observed X-ray cluster gas abundance and the former is chosen to match the observed GSWs (see, e.g., Pettini et al. 2002). In other words, our model is basically free of adjustable parameters other than overall yield and $e_{\rm GSW}$, and

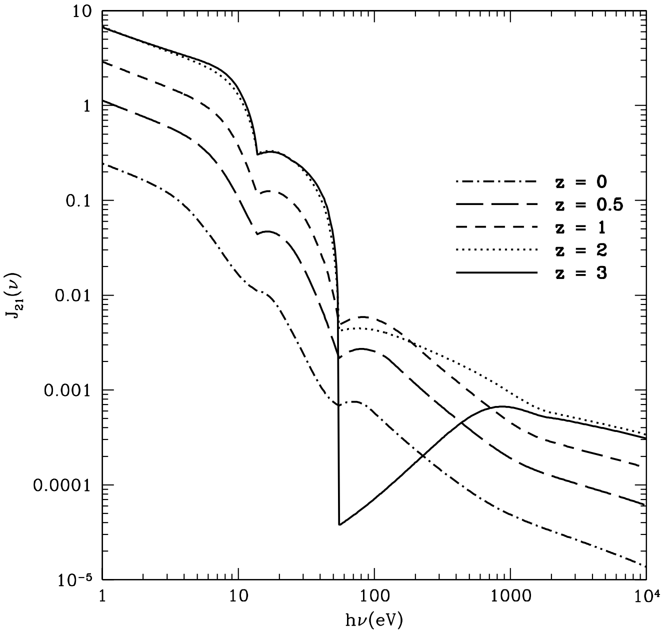

FIG. 1.—The background radiation field in units of 10^{-21} ergs cm^{-2} s^{-1} sr^{-1}, at five redshifts, z = 3, 2, 1, 0.5, and 0, computed in our simulations. [*See the electronic edition of the Journal for a color version of this figure.*]

it is fair to say that the excellent agreement between our calculation and observations is a strong indication that our cosmological model is a faithful representation of the true universe in this regard.

However, the excellent agreement would not have been found had the effect of GSWs not been included (*vertically hatched curve*) or if we had adopted the equilibrium (Cloudy) treatment (*horizontally hatched curve*). Both GSW feedback and the nonequilibrium method produce significant errors for abundances of low equivalent width absorption lines (EW $\leq$ 30 Å). One may fortuitously obtain an apparently reasonable agreement between theoretical calculations and observations if both errors in modeling are simultaneously made, that is, an equilibrium Cloudy treatment in a simulation with no significant GSW feedback; this is a mere coincidence. The physical reason why the equilibrium treatment produces more O VI than the nonequilibrium simulation is that collisional ionization timescales are longer than the timescale on which gas is shock-heated, especially for low-density regions; for the very high density regions, the two approaches should agree, as Figure 2 indicates. The results obtained here are broadly consistent with earlier simulations (Cen et al. 2001; Fang & Bryan 2001; Chen et al. 2003) and with analytic work (Furlanetto et al. 2005a) with regard to O VI absorption line abundance, taking into account various uncertainties about cosmological model parameters, different treatments of metallicity, and assumptions about ionization equilibrium.

Figure 3 shows the number of O VII absorption lines per unit redshift as a function of equivalent width from simulations with (*solid curve*) and without (*vertically hatched curve*) GSWs. Also included (*horizontally hatched curve*) is what one would obtain using Cloudy based on the simulation with GSWs. Somewhat different from the case for O VI, we see here that the feedback and nonequilibrium effects each produce a 30%–50% change, in the

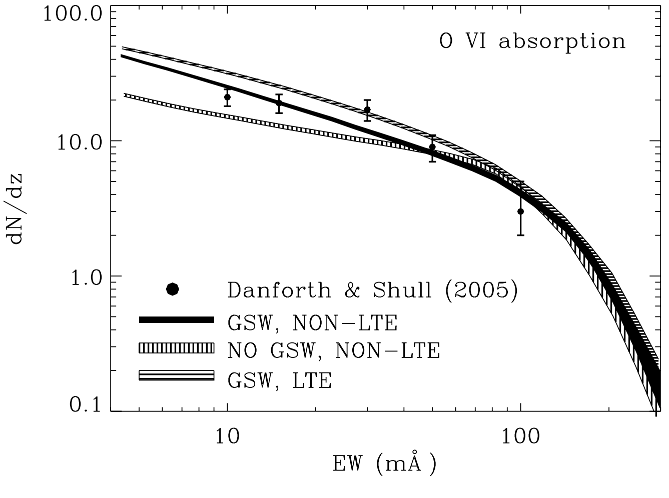

FIG. 2.—Number of O VI absorption lines per unit redshift as a function of equivalent width in units of milliangstroms. The solid curve shows our primary results from the simulation with GSWs, and the vertically hatched curve shows results from the simulation without GSWs. The horizontally hatched curve was computed using Cloudy under the assumption of ionization equilibrium based on the density, temperature, and metallicity information from the simulation with GSWs. The filled circles are observations by Danforth & Shull (2005). [*See the electronic edition of the Journal for a color version of this figure.*]

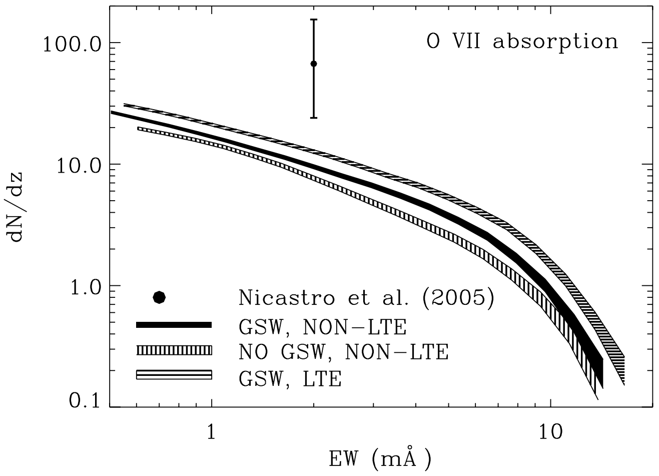

FIG. 3.—Same as Fig. 2, but for O VII. The filled circle is an observation by Nicastro et al. (2005). [*See the electronic edition of the Journal for a color version of this figure.*]

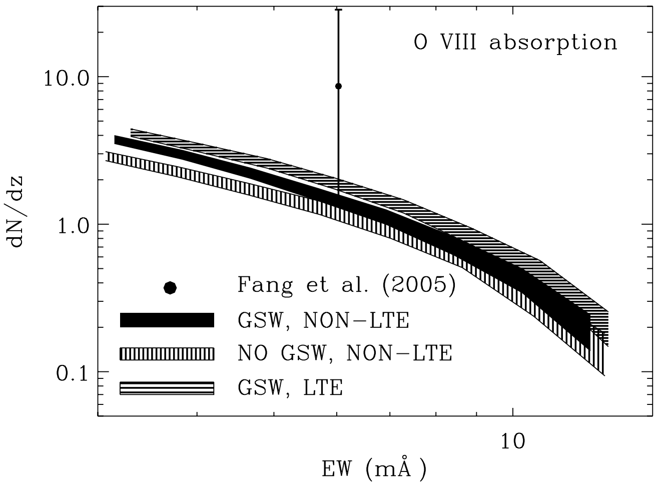

FIG. 4.—Same as Fig. 2, but for O VIII. The filled circle is an observation by Fang et al. (2005). [*See the electronic edition of the Journal for a color version of this figure.*]

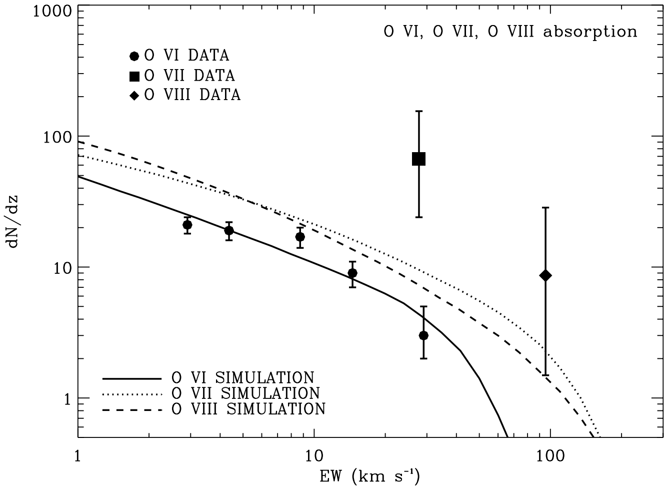

Fig. 5.—Number of all three absorption lines, O vi (*solid curve*), O vii (*dotted curve*), and O viii (*dashed curve*), per unit redshift as a function of equivalent width in units of kilometers per second, from the simulation with GSWs. The symbols are observations by Danforth & Shull (2005), Nicastro et al. (2005), and Fang et al. (2005) for O vi, O vii, and O viii absorption lines, respectively. [*See the electronic edition of the Journal for a color version of this figure.*]

opposite direction, in the predicted number of O vii absorption lines for the entire range of equivalent widths. Figure 4 is similar to Figure 3, but for O viii absorption lines, and comparable effects due to GSWs and equilibrium treatment are seen. In both cases, for O vii and O viii absorption lines the agreement between observations and our detailed nonequilibrium calculations with GSWs are not as good as that for the O vi absorption line seen in Figure 2. However, the observational error bars for the abundances of these two absorption lines are currently very large because of the very small observational sample. The physical reason behind the results that the equilibrium treatment produces more O vii and O viii than the nonequilibrium simulation is similar to that given for the case of O vi, except that the collisional ionization timescales are still longer in the case of O vii and O viii and the timescales on which gas is shock-heated are still shorter than for O vi, as Figure 2 indicates. It will be of great importance to enlarge the observational samples for both O vii and O viii absorption lines, to make comparisons that are more statistically sound. Since our model has no adjustable parameters except yield and $e_{\rm GSW}$, the outcome from such comparisons will provide critical tests of yield, $e_{\rm GSW}$, and the underlying cosmological model.

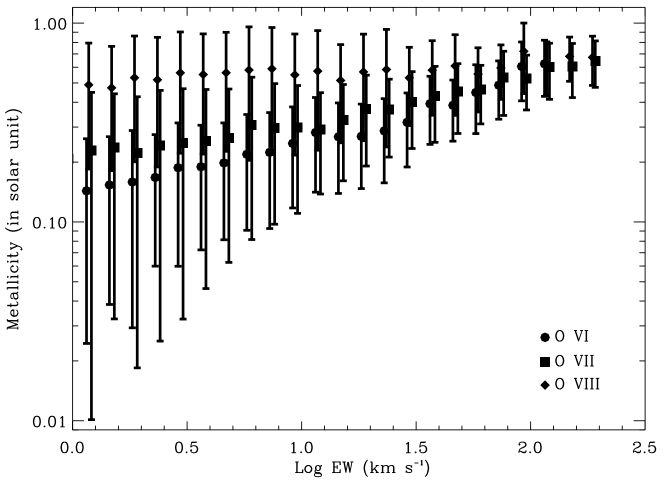

Fig. 6.—Average metallicity of O vi, O vi, and O viii absorption lines as a function of equivalent width. The error bars indicate the scatter about the average. [*See the electronic edition of the Journal for a color version of this figure.*]

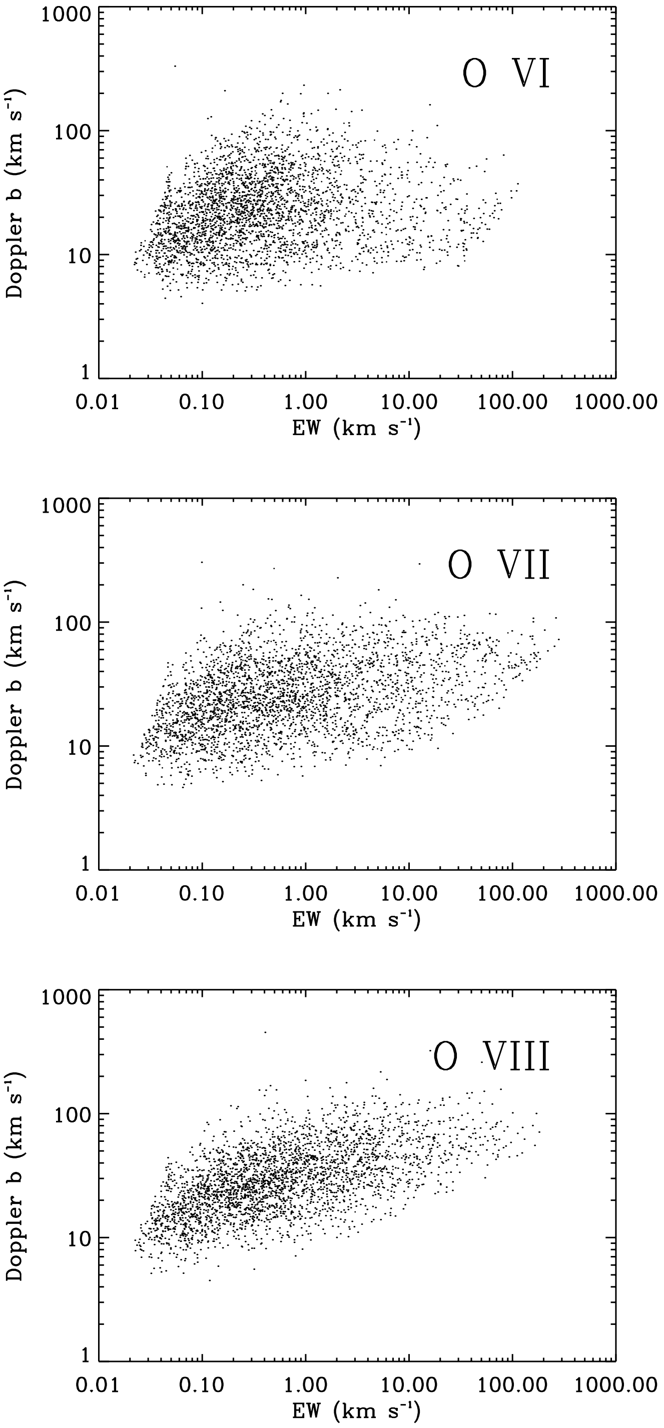

Fig. 7.—Doppler *b*-parameter of lines vs. their equivalent widths, for O vi (*top*), O vii (*middle*), and O viii (*bottom*).

To summarize the relative abundances of these major species, Figure 5 displays results for all three absorption lines in terms of equivalent width in units of kilometers per second to indicate the relative abundances of the three major species. The conversion between EW in milliangstroms and EW in kilometers per second is $\mathrm{EW(m\AA)} = \lambda \times \mathrm{EW(km\ s^{-1})}/c$, which is equal to $(34.3\ \mathrm{m\AA})[\mathrm{EW(km\ s^{-1})}/(10\ \mathrm{km\ s^{-1}})]$, $(0.35\ \mathrm{m\AA})[\mathrm{EW(km\ s^{-1})}/(50\ \mathrm{km\ s^{-1}})]$, and $(0.32\ \mathrm{m\AA})[\mathrm{EW(km\ s^{-1})}/(50\ \mathrm{km\ s^{-1}})]$, for O vi,

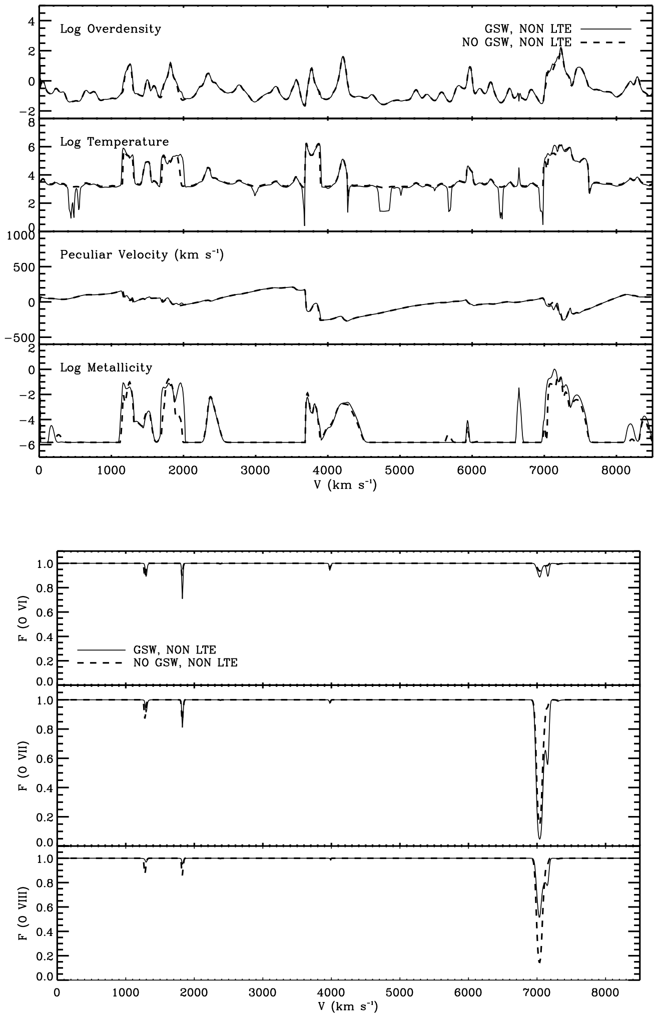

FIG. 8.—One line of sight through the simulation box. The top four panels, from top to bottom, show gas overdensity, temperature, peculiar velocity, and metallicity (in solar units). The bottom three panels, from top to bottom, are flux absorption spectra for O vi, O vii, and O viii lines, respectively. The solid curves are for the simulation with GSWs, and the dashed curves are for that without GSWs. [*See the electronic edition of the Journal for a color version of this figure.*]

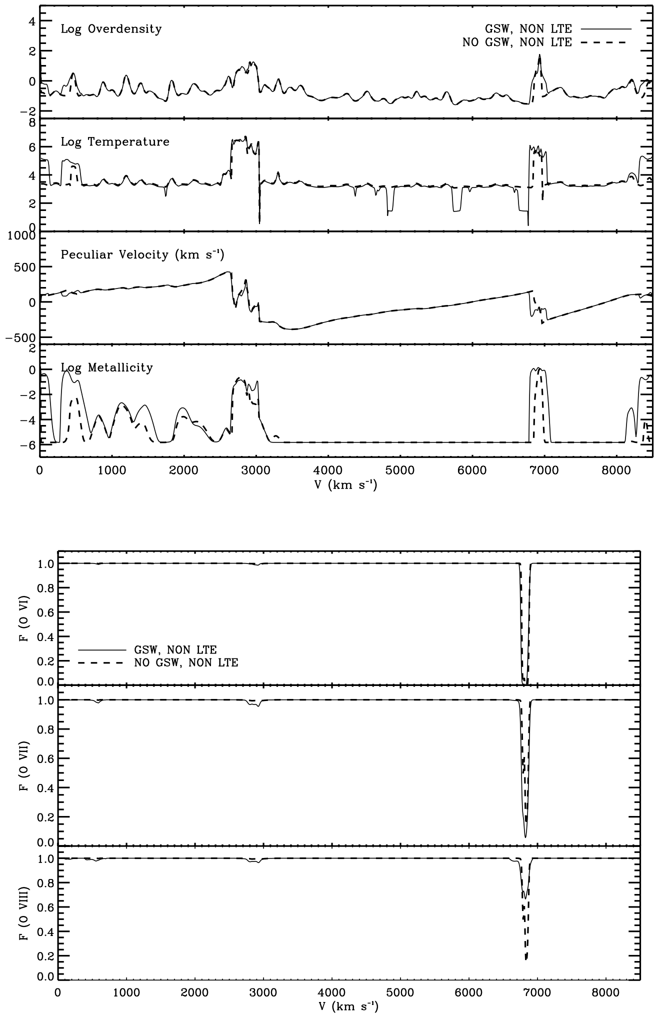

FIG. 9.—Same as Fig. 8, for another line of sight through the simulation box. [*See the electronic edition of the Journal for a color version of this figure.*]

O vii, and O viii, respectively. The expected abundances for these three lines are in the range 50–100 per unit redshift at EW = 1 km s^{-1}, decreasing to 10–20 per unit redshift at EW = 10 km s^{-1}; the rate of decrease of the line abundance at higher EW then becomes significantly higher. The number of O vi absorption lines with EW > 100 km s^{-1} is very small, while there are about one to three lines per unit redshift for O vii and O viii absorption lines at EW = 100 km s^{-1}. The computed O vii and O viii absorption line abundances are in reasonable agreement with Chen et al. (2003), in particular, for their "scatter" metallicity model (their Fig. 7, *dashed curve*), considering the large uncertainties in the metallicity distribution and the assumption of ionization equilibrium.

Figure 6 shows the average metallicity (with scatter) of O vi, O vi, and O viii absorption lines as a function of equivalent width. We see two clear trends, albeit with significant scatter: (1) At low EW, O vi absorption lines have on average the lowest metallicity, while O viii absorption lines have the highest metallicity. (2) For each absorption line, higher EW lines have higher metallicity. Overall, on average, O vi lines have a metallicity range of 0.15–0.60 $Z_\odot$, with large scatter at the low end. The O vii absorption lines have a mean metallicity range of 0.20–0.60 $Z_\odot$ with somewhat larger scatter at the low end than the O vi line. The O viii absorption lines, quite interestingly, display a nearly constant mean metallicity of ∼0.5–0.6 $Z_\odot$ over the entire EW range. All three absorption lines converge to a mean metallicity of 0.6 $Z_\odot$ at the high-EW end, with a scatter of about 0.2 $Z_\odot$.

Figure 7 shows the Doppler width b as a function of EW for O vi, O vii, and O viii. One can see that the Doppler widths for the three species all have a concentration broadly in the range of 10–60 km s^{-1} at the low-EW end. This suggests that peculiar-velocity effects play a very important role here. It should be noted that peculiar velocities affect widths in complex ways, either broadening or narrowing depending on the details of the velocity and shock structures. In some cases, Hubble expansion could counter the effect of the peculiar velocities of enclosing double shocks. Most of the very low b structures are likely photoionized, and the overall velocity-broadening effect is minimal. On the high-EW end, the trend is somewhat more clear. There, the b-values of O vi, O vii, and O viii appear to increase more or less monotonically, in that order. This is due to the fact that higher ionization species are closer to the center of potential wells and thus have, on average, higher temperatures and velocities.

Finally, Figures 8–10 show in detail three randomly chosen lines of sight through the simulation boxes that have significant absorption features. Notable features in these figures are the following:

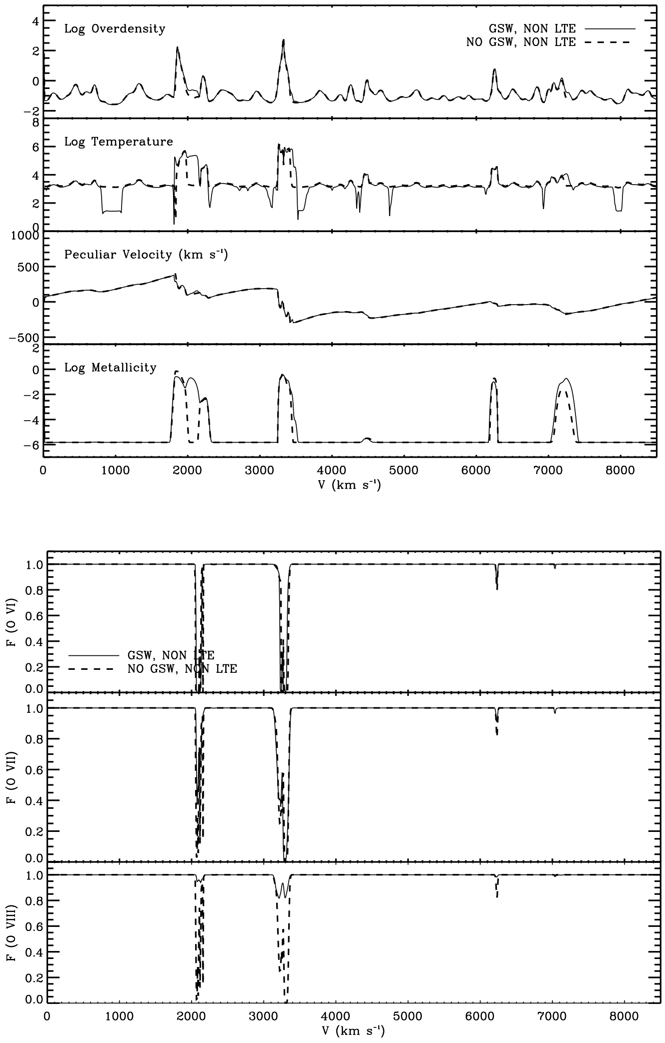

FIG. 10.—Same as Fig. 8, for yet another line of sight through the simulation box. [*See the electronic edition of the Journal for a color version of this figure.*]

(1) GSWs in most cases tend to broaden the absorption-line profiles. (2) GSWs may alter the absorption profile in complex ways, as clearly seen in the bottom two panels of Figure 8 for O VII and O VIII, thanks to a combination of separate effects on the gas velocity, temperature, metallicity, and density. (3) The typical gas density of the absorption features seen is in the range of 10–300 times the mean gas density. (4) The typical metallicity of gas producing the prominent UV absorption lines is in the range 0.1–1.0 $Z_\odot$. (5) The significant absorption features are usually enclosed by double shocks with velocities in the range 100–400 km s^{-1}, that is, we are seeing the outer edges of a cooling "Zel'dovich pancake." In fact, such a pattern has been detected in a cluster of multiphase absorbers along the sight line toward PKS 2155−304 (Shull et al. 2003). We note that a multiphase medium, while common, most often does not have spatially coexisting components; rather, complex velocity, density, and metallicity structure mask their appearances when observed in Hubble space. (6) The Doppler line widths for deep lines are 100–300 km s^{-1}, while for more abundant small lines the widths are small, in the range of 1–100 km s^{-1}. (7) The relative absorption strengths of the three considered lines vary, and no particular order is visible, as expected, since the line strengths are functions of several physical variables. We defer more detailed studies to a subsequent paper.

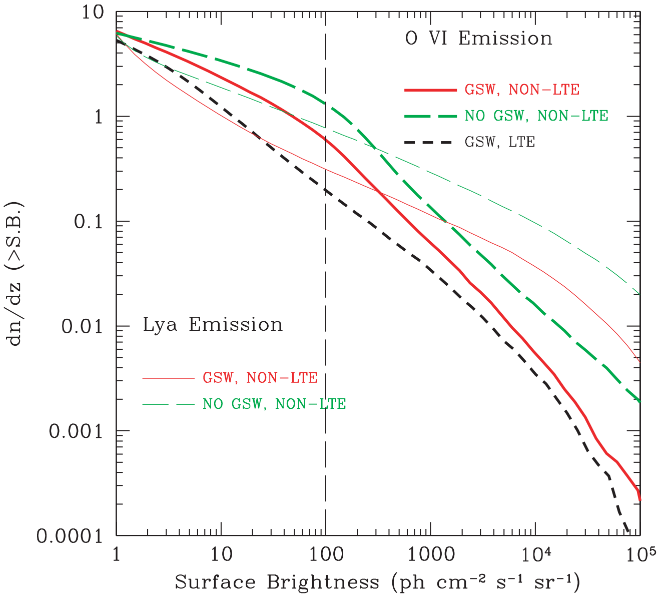

FIG. 11.—Cumulative number of O VI (*thick curves*) and Lyα (*thin curves*) lines per unit redshift as a function of surface brightness. The solid curves show results from the simulation with GSWs, and the dashed curves those from the simulation without GSWs. The short-dashed curve (for O VI only) was computed using Cloudy under the assumption of ionization equilibrium based on the density, temperature, and metallicity information from the simulation with GSWs. Note that future planned UV missions may be able to achieve a sensitivity in the range of 100 in the displayed units, as indicated by the dashed vertical line. [*See the electronic edition of the Journal for a color version of this figure.*]

3.2. *Emission Lines in UV and X-Rays*

In order to directly map out the WHIM structure in three dimensions, detailed emission measurements are invaluable, because of their potential for continuous coverage and a lack of dependence on the sparsely distributed background sources required for absorption studies. We will focus on three metal emission lines, O VI, O VII, and O VIII, as well as the Lyα emission line. Emission tables were generated using the software package CHIANTI,[4] based on the electron density and density of a specific metal species. Emission lines are identified as follows: First, we compute the emissivity of each cell for a chosen metal line using an emission table. Second, we project the simulation box along each of the three orthogonal axes to produce a two-dimensional map with pixel size equal to the simulation cell size. Third, we find emission lines as a function of surface brightness in each two-dimensional map. This simple procedure is tested and works very well, because overlapping of emission lines at different redshifts along a line of sight of depth equal to the size of the simulation box is very rare.

Figure 11 shows the cumulative number of O VI and Lyα lines in the UV per unit redshift as a function of surface brightness. We have assumed that an applicable telescope has a spatial resolution that is smaller than our simulation cell size, and in this case the plotted quantity in Figure 11 and the following figures is independent of the telescope's spatial resolution. The solid curves show results from the simulation with GSWs, and the long-dashed curves those from the simulation without GSWs. The short-dashed curve (for O VI only) was computed using Cloudy under the assumption of ionization equilibrium based on the density, temperature, and metallicity information from the simulation with GSWs. The results found with regard to Lyα emission may be compared with Figure 8 of Furlanetto et al. (2005b). Their

---

[4] See http://www.solar.nrl.navy.mil/chianti.html.

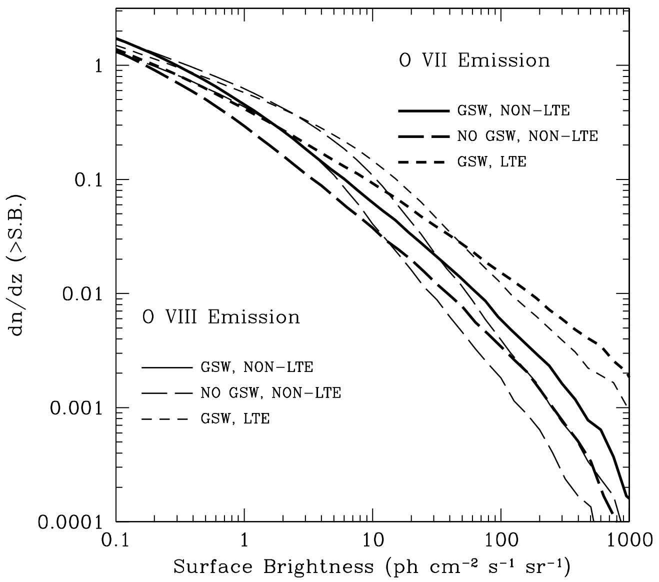

FIG. 12.—Same as Fig. 11, but for O VII (*thick curves*) and O VIII (*thin curves*). The planned Japanese soft X-ray mission *DIOS* (Yoshikawa et al. 2003) will have a sensitivity of order 0.1 in the displayed units. [*See the electronic edition of the Journal for a color version of this figure.*]

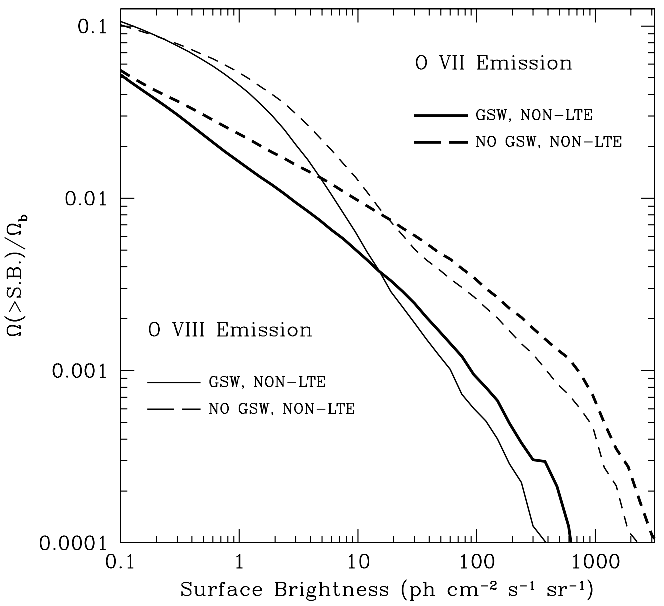

FIG. 14.—Same as Fig. 13, but for O VII (*thick curves*) and O VIII (*thin curves*). [*See the electronic edition of the Journal for a color version of this figure.*]

figure has different units for the ordinate, while the abscissa has the same units. In order to convert the values of the ordinates in their Figure 8 to dn/dz as displayed here, we need to multiply by $(dl/dz)/\delta l = 4478$, where $\delta l = 0.67\ h^{-1}$ Mpc is their pixel depth and $dl/dz = 3000\ h^{-1}$ Mpc is the length per unit redshift at $z = 0$. Good agreement is found between their results and ours. For example, at a surface brightness of $\phi = 10^2$ photons cm^{-2} s^{-1} sr^{-1}, we find $dn/dz(>\phi) = 0.33$ (Fig. 11, *thin solid curve*), while their values range from 0.11 (their Fig. 8*b*) to 0.70 (their Figs. 8*a* and 8*c*). Also, we may compare the results found in regard to O VI emission with Figure 9 of Furlanetto et al. (2004), which shows the probability distribution function (defined as $dn/d \ln \phi$ for $\delta z = 0.01$) of O VI emission. Integrating, for example, the dotted curve in their Figure 9*c*, we find their $dn/dz(>\phi) = 0.40$ at a surface brightness of $\phi = 10^2$ photons cm^{-2} s^{-1} sr^{-1}, which should be compared with our value of 0.61 (Fig. 11, *thick solid curve*). At face value, their emission estimate is somewhat lower than ours, but the difference should be considered small, given the many physical and numerical factors involved. Therefore, we instead consider this to be good agreement.

Figure 12 shows a similar plot for the O VII and O VIII lines in soft X-rays. Note that future planned UV missions (for O VI and Lyα lines) may be able to achieve a sensitivity in the range of 100 in the displayed units, and the proposed soft X-ray missions (for O VII and O VIII lines: the *Diffuse Intergalactic Oxygen Surveyor* [*DIOS*; Yoshikawa et al. 2003] and *Missing Baryon Explorer* [*MBE*; Fang et al. 2005]) are expected to be able to

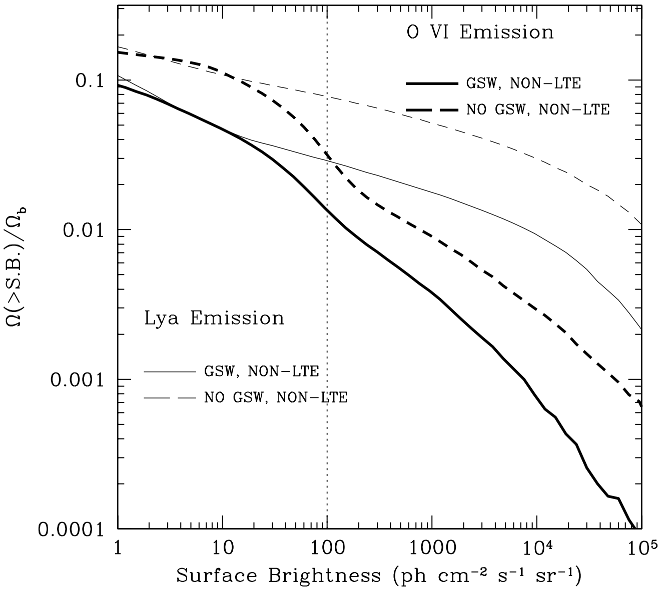

FIG. 13.—Cumulative gas mass density probed by the O VI (*thick curves*) and Lyα (*thin curves*) lines as a function of surface brightness. The solid curves show results from the simulation with GSWs, and the dashed curves those from the simulation without GSWs. [*See the electronic edition of the Journal for a color version of this figure.*]

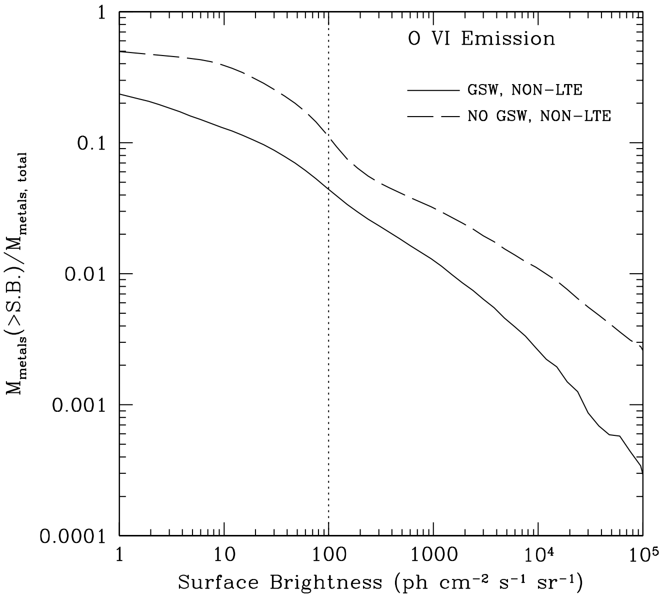

FIG. 15.—Cumulative metal mass probed by the O VI line as a function of surface brightness. The solid curve shows results from the simulation with GSWs, and the dashed curve those from the simulation without GSWs. [*See the electronic edition of the Journal for a color version of this figure.*]

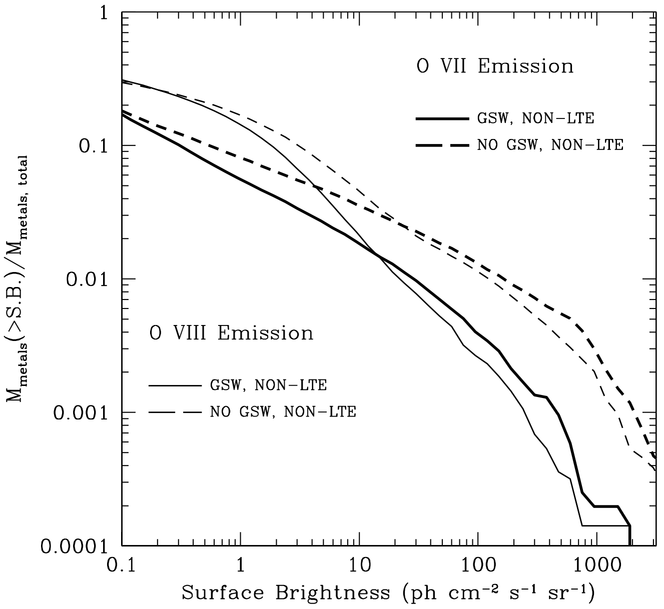

Fig. 16.—Same as Fig. 15, but for O vii (*thick curves*) and O viii (*thin curves*). [*See the electronic edition of the Journal for a color version of this figure.*]

achieve a sensitivity of order 0.1 in the displayed units for a reasonable amount of exposure time. We see that both UV emission lines, such as Lyα and O vi, and soft X-ray emission lines, such as O vii and O viii, have comparable abundances. The number of emission lines per unit redshift that may be detectable by the planned UV and soft X-ray missions are of order 0.1–1. Therefore, it is highly desirable to be able to map out emission in both the UV and X-ray bands, because they often probe complementary physical regions.

How large a fraction of the baryons may be probed by these metal emission lines? Figures 13 and 14 show the total amount of baryons that can be probed by emission lines as a function of surface brightness. For the quoted sensitivities, in the range 100–1000 in the displayed units, we see that the O vi line may be able to probe about 0.5%–1.5% of all baryons, or 1%–3% of the WHIM, while Lyα may be able to probe about 4%–6% of the WHIM. The *DIOS* and *MBE* X-ray missions are expected to be able to detect 10% and 20% of the WHIM using O vii and O viii lines, respectively, which may be compared with calculations by Yoshikawa et al. (2004), who found that at 10^{-10} ergs s^{-1} cm^{-2} sr^{-1} (which corresponds to our adopted *DIOS* and *MBE* sensitivity of $\phi = 0.1$ photons cm^{-2} s^{-1} sr^{-1}), the WHIM mass fractions probed by O vii and O viii are 18% and 20%, respectively. Given the difference between our treatment and theirs, this agreement should be considered good, and this also suggests that the local universe, as they simulated, represents a fair sample of the universe with regard to the WHIM. Since metal enrichment of the IGM is quite inhomogeneous, these emission lines, being in overdense regions, should be able to track a larger fraction of metals produced in star formation. Figures 15 and 16 show that the O vi emission line will be able to probe about 1.5%–4% of all metals in the IGM, while the O vii and O viii emission lines will be able to probe about 15%–30% of all metals in the IGM. In all the above figures (Figs. 11–16), we show that GSWs affect the quantitative results dramatically; omission of the GSW effect could cause errors of 100%–1000% with regard to line abundances, baryonic densities, and metal densities.

Figures 17 and 18 show the observable regions of the sky (*black*) in a map of size 85 × 85 h^{-2} Mpc^2 using O vi and Lyα lines, respectively, for an instrument with a sensitivity of 100 photons cm^{-2} sr^{-1} s^{-1}. Figures 19 and 20 show the same using O vii and O viii lines, respectively, for an instrument with a sensitivity of

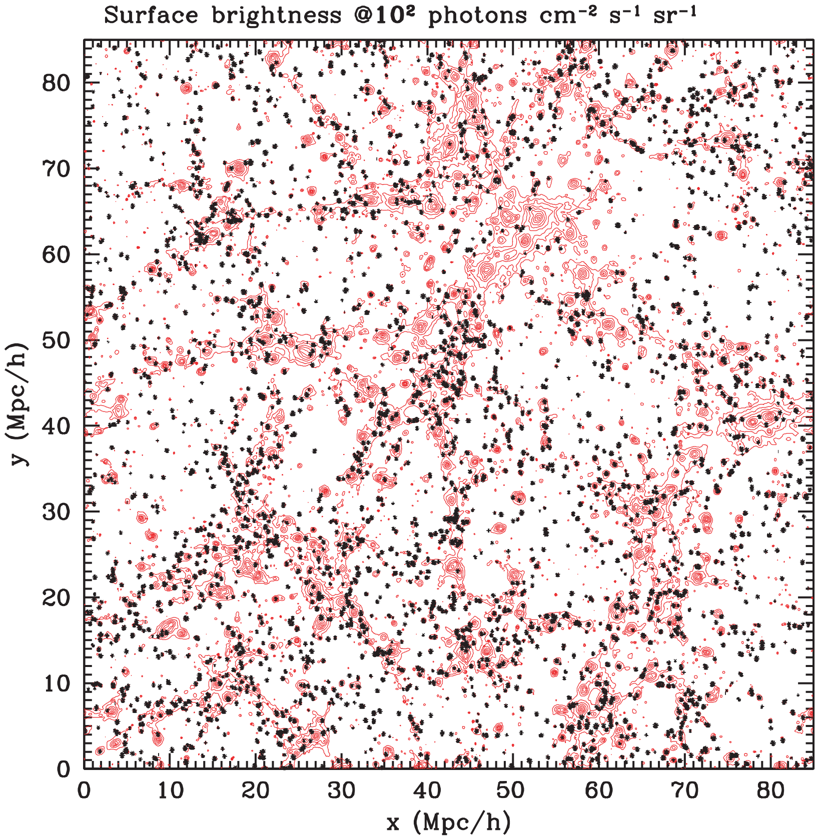
Surface brightness @10^2 photons cm^{-2} s^{-1} sr^{-1}
y (Mpc/h)
x (Mpc/h)
0
10
20
30
40
50
60
70
80

Fig. 17.—A map of size 85 × 85 h^{-2} Mpc^2 and depth 85 h^{-1} Mpc, with the observable regions shown as black spots for the O vi emission line for an instrument with a sensitivity of 100 photons cm^{-2} sr^{-1} s^{-1}. The red contours are the underlying gas density distribution.

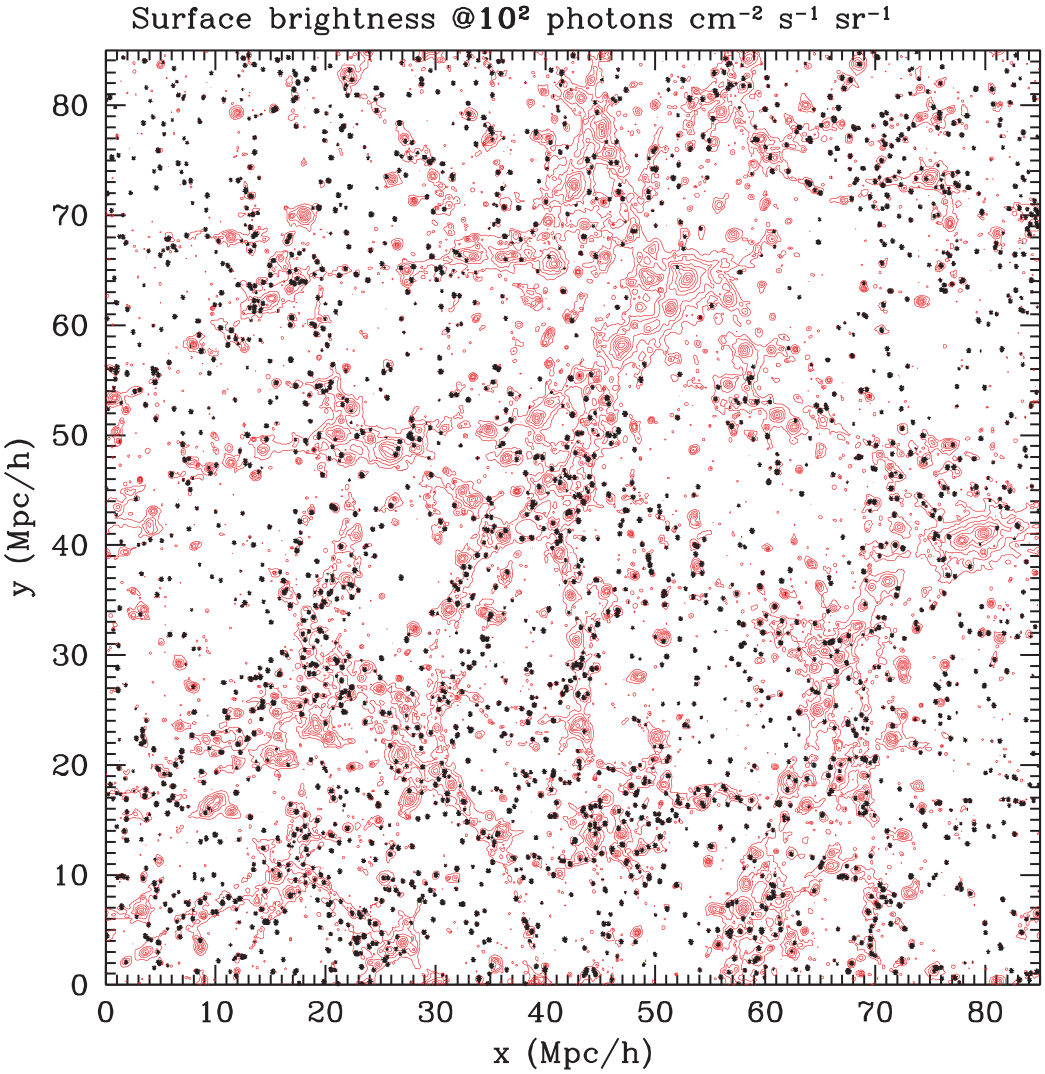

FIG. 18.—Same as Fig. 17, but for Lyα emission.

0.1 photons cm^{-2} sr^{-1} s^{-1} (*DIOS*). The red contours are the underlying gas density distribution. It is quite clear that while the regions detectable by these UV and soft X-ray emission lines cannot continuously cover the entire filamentary network, they provide a faithful representation of the underlying density structure, especially the filaments. It may be noted that O VI and Lyα provide a rather poor tracer for some of the larger concentrations of red contours, because the latter are sites of hotter gas in the WHIM temperature range, too hot to be traceable by these UV emission lines; the O VII and O VIII X-ray emission lines provide a relatively better set of probes for this hot gas. Figures 21–24 zoom in to a smaller region of Figures 17–20, respectively, to better display the detailed correspondence between detectable regions and the underlying density structure. We see that both O VI and Lyα lines tend to avoid the larger density knots and often appear to be off-center, that is, located in the outskirts of large density concentrations. In contrast, the O VII and O VIII emission lines most often directly overlap the larger density concentrations and do not probe their outskirts. This clearly illustrates the complementarity of missions to observe UV and X-ray emission, dictated by the complex physical structure of the WHIM in the vicinity of galaxies and groups of galaxies. The physical variables that play important roles here are gas temperature, gas density, gas metallicity, and gas peculiar velocity. None of these can be tracked simply, but all of them are expected to be influenced significantly by GSWs. Therefore, detailed comparisons between simulations and observations, when the become available, may provide an extremely valuable tool to probe galaxy formation and its all-important feedback processes.

4. DISCUSSION AND CONCLUSIONS

In Cen & Ostriker (2006), we showed that our significantly improved simulations confirm previous conclusions based on earlier simulations: *nearly half of all baryons at the present epoch should be found in the WHIM*—a filamentary network in the temperature range of 10^5–10^7 K. There, we also presented significant effects due to feedback from star formation.

Here we have investigated detailed ionization distributions of oxygen, computed explicitly in a nonequilibrium way, and presented results that relate to important UV and soft X-ray lines and how observations of them may shed light on the WHIM and galaxy formation processes. Our findings are as follows: (1) Nonequilibrium calculations produce significantly different results than do equilibrium calculations, and the differences are complex and difficult to characterize simply. (2) The abundance of O VI absorption lines based on nonequilibrium simulations with galactic superwinds is in remarkably good agreement with the latest observations, implying the validity of our model, while the

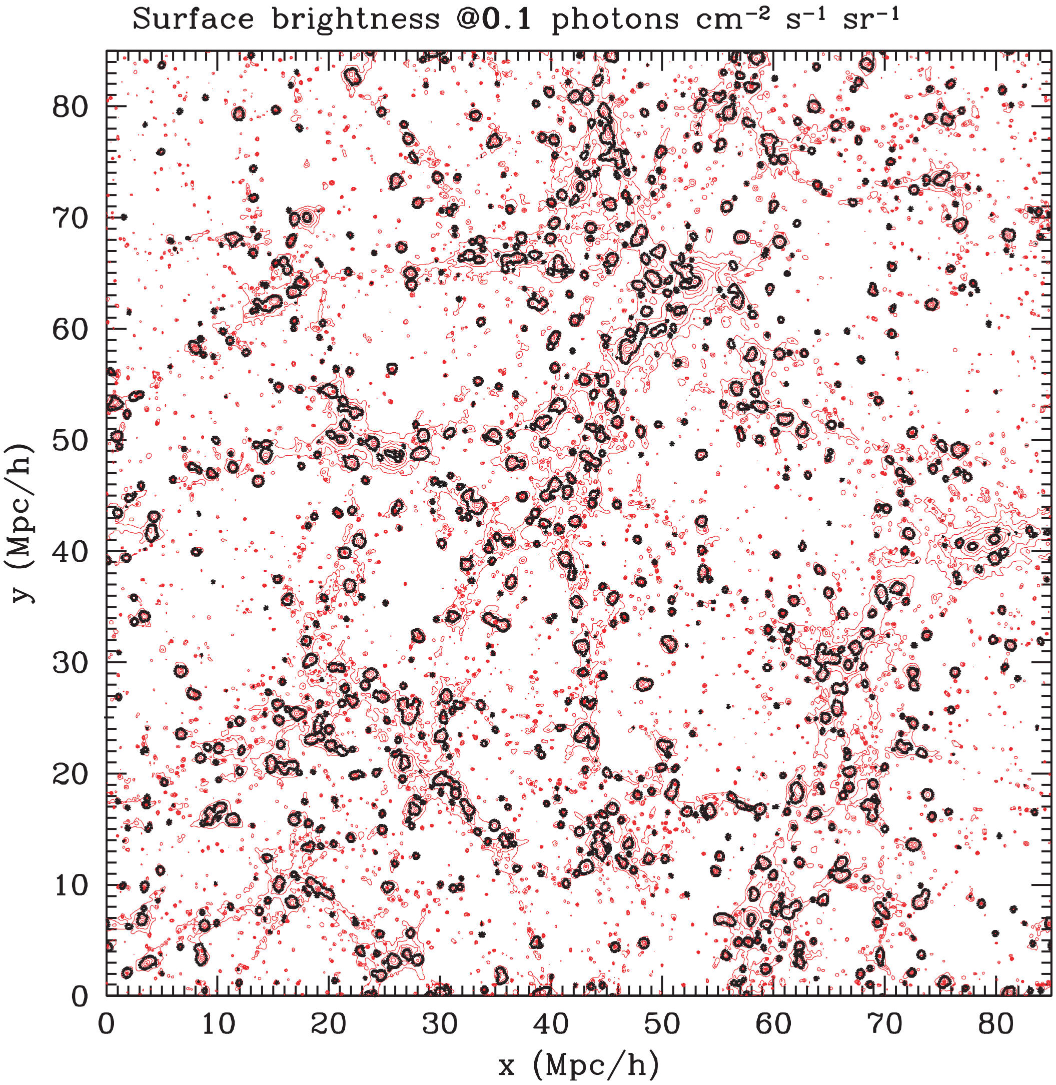

FIG. 19.— Same as Fig. 17, but for the O VII emission line and an instrument with a sensitivity of 0.1 photons cm^{-2} sr^{-1} s^{-1}.

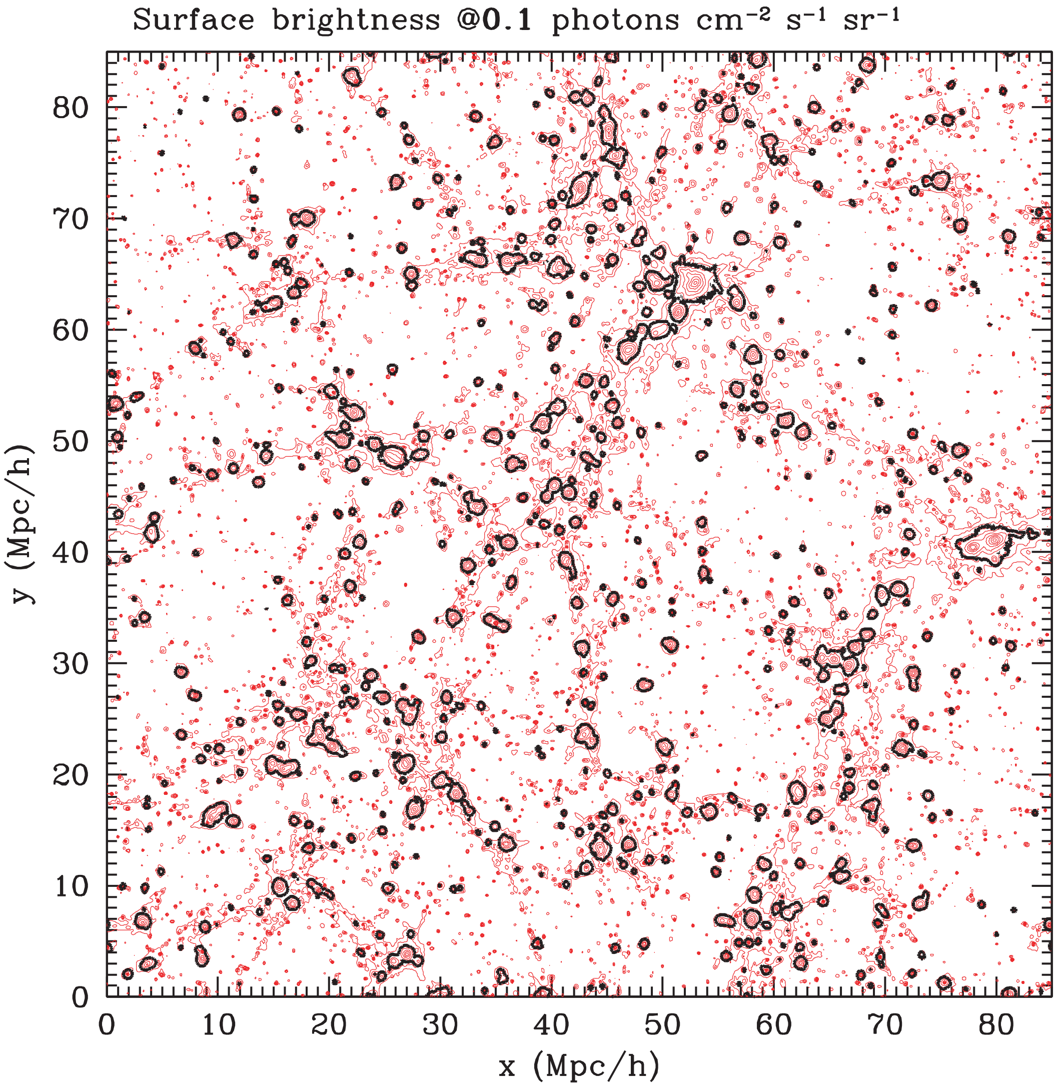

FIG. 20.—Same as Fig. 17, but for the O VIII emission line and an instrument with a sensitivity of 0.1 photons cm^{-2} sr^{-1} s^{-1}.

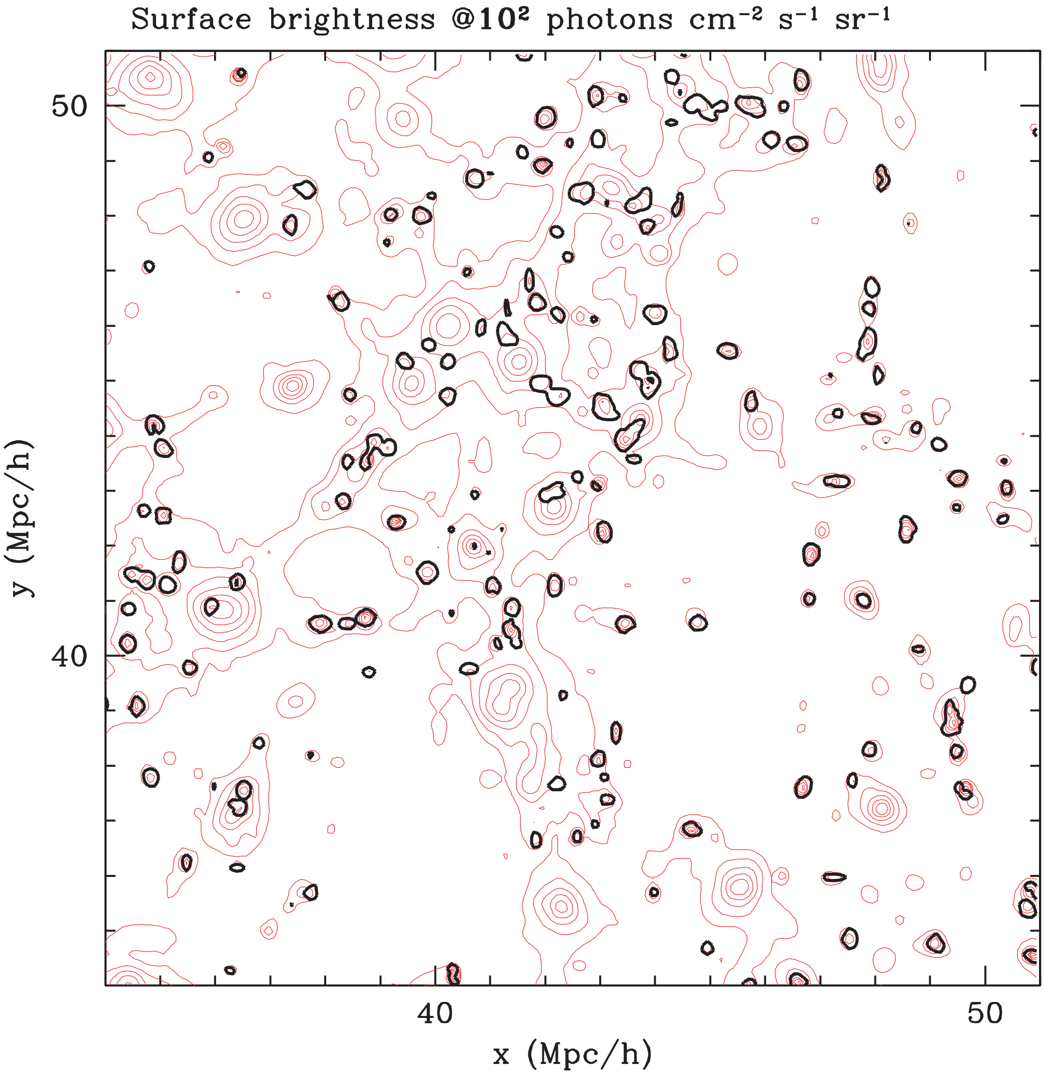

FIG. 21.—Enlargement of a part of Fig. 17, to better display some details.

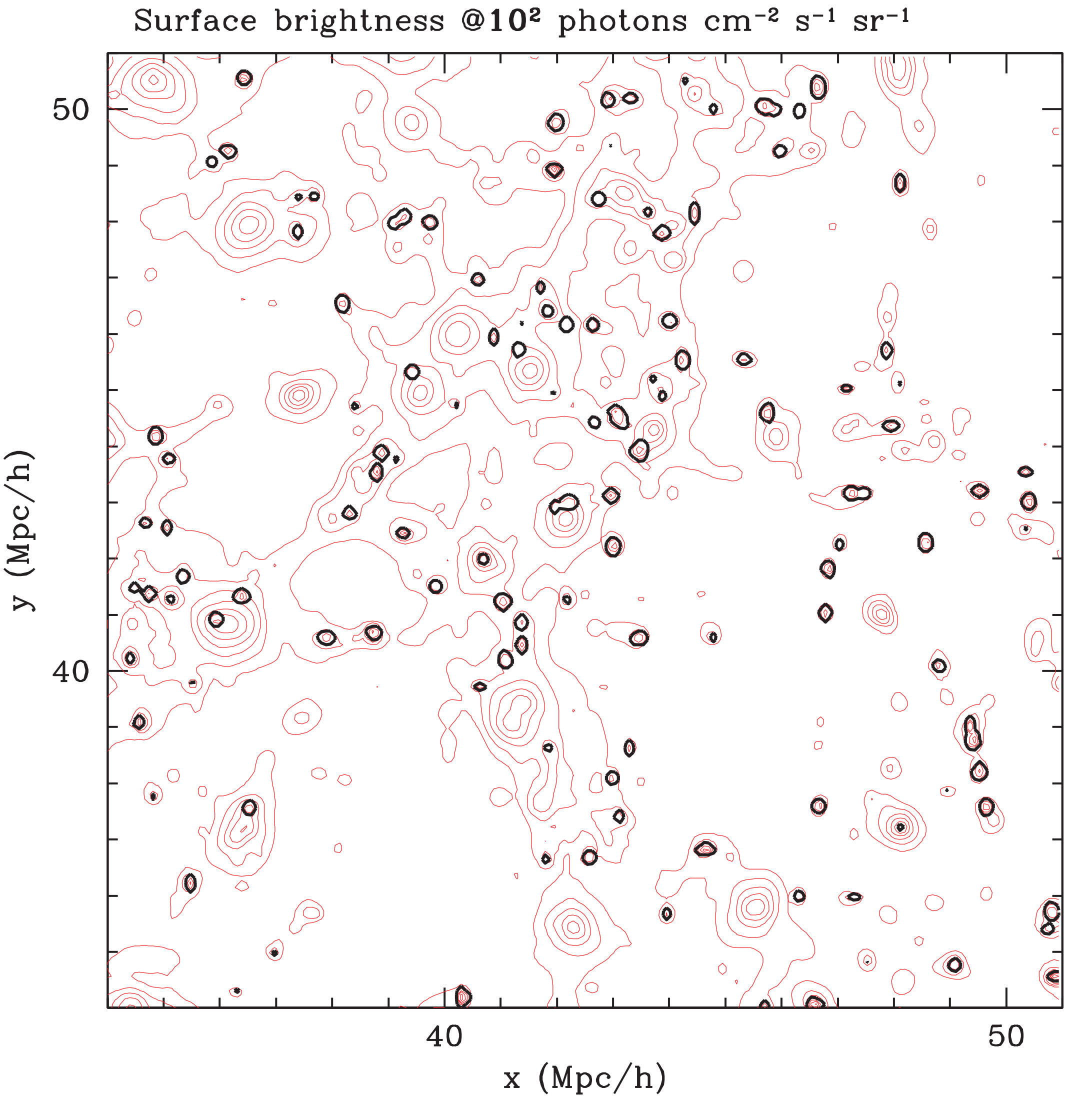

FIG. 22.—Enlargement of a part of Fig. 18.

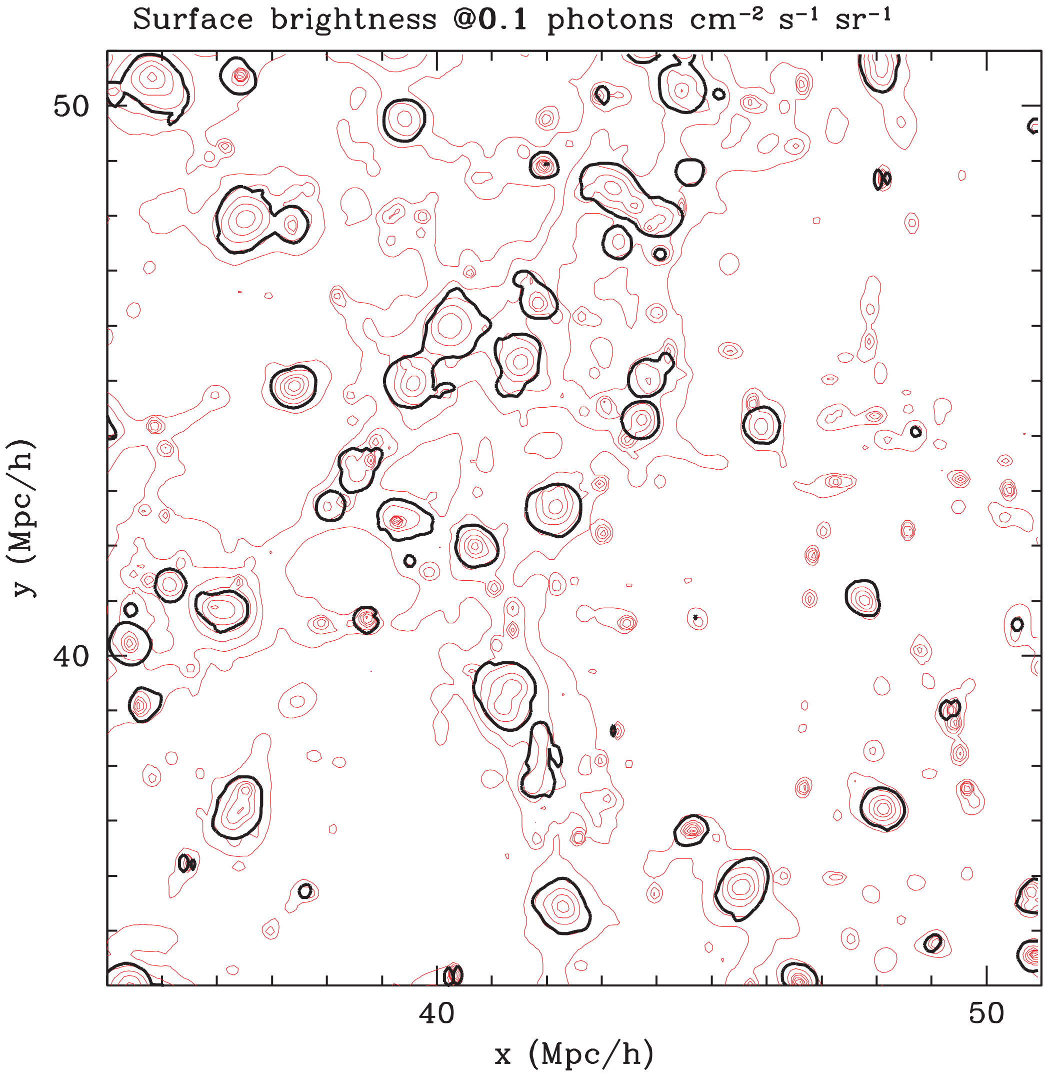

FIG. 23.—Enlargement of a part of Fig. 19.

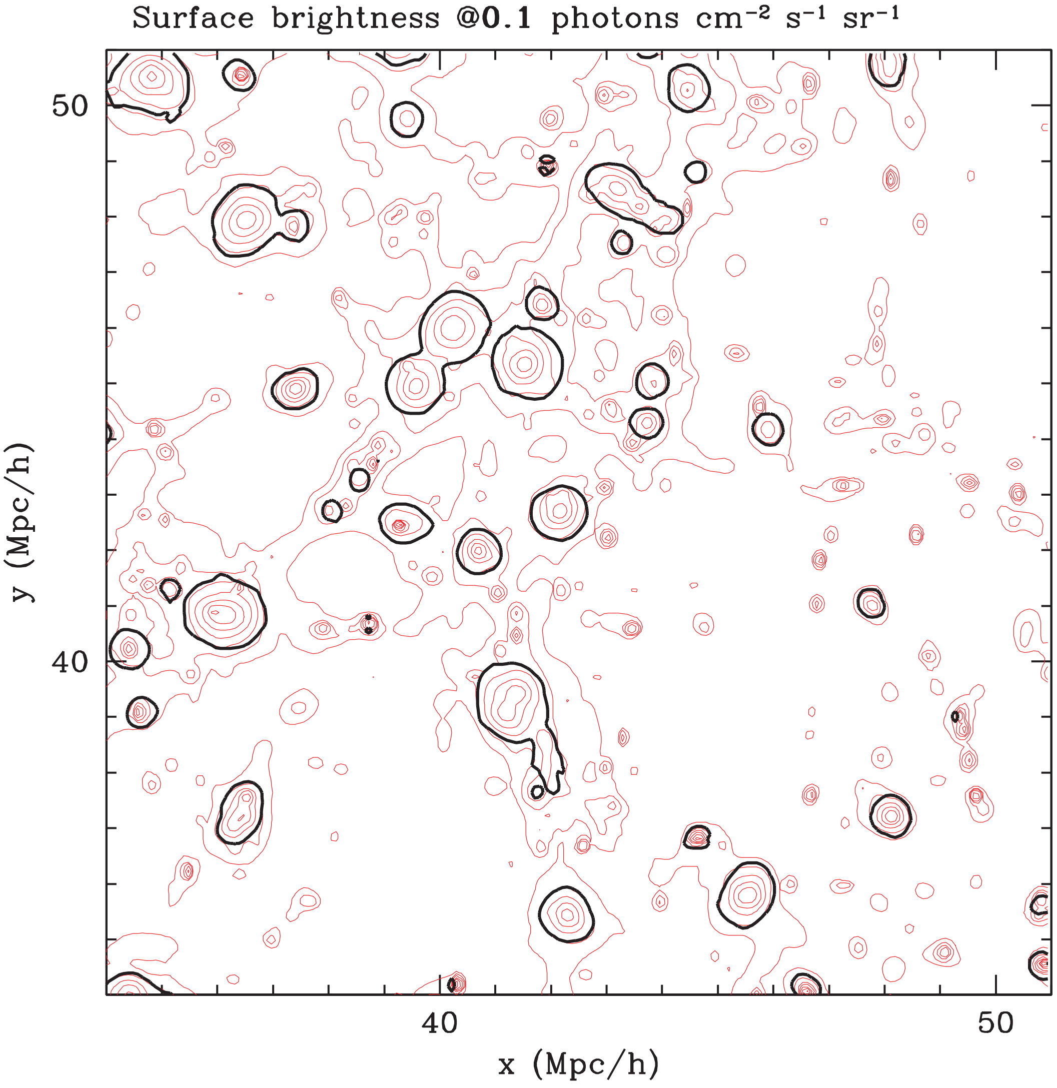

FIG. 24.—Enlargement of a part of Fig. 20.

predicted abundances for O vii and O viii absorption lines appear to be lower than observed, although the observational error bars are currently very large. The expected abundances for O vi (as well as Lyα), O vii, and O viii lines are in the range 50–100 per unit redshift at EW = 1 km s^{-1}, decreasing to 10–20 per unit redshift at EW = 10 km s^{-1}. The number of O vi absorption lines with EW > 100 km s^{-1} is very small, while there are about one to three lines per unit redshift for O vii and O viii absorption lines at EW = 100 km s^{-1}. (3) Emission lines, primarily O vi and Lyα in the UV and O vii and O viii in soft X-rays, are potentially observable by future missions, and they provide complementary probes of the WHIM in often different domains in the temperature-density-metallicity phase space, as well as in different spatial locations; however, sometimes they overlap spatially and in phase space, making joint analyses very useful. The number of emission lines per unit redshift that may be detectable by planned UV and soft X-ray missions are of order 0.1–1.

We expect that future UV and X-ray missions should be able to provide a much more accurate characterization of the WHIM through two complementary approaches: major UV and soft X-ray absorption lines and emission lines. The former will be able to trace out the bulk of the mass, as well as the volume occupied, by the WHIM, whereas the latter will be able to probe higher density regions. Together they may allow us to construct a coherent picture of the evolution of the IGM. In addition, detailed and useful information may be obtained by investigating the relations between galaxies and properties of the WHIM, keeping in mind that GSWs play an essential role in exchanging mass, metals, and energy between them. We stress that proper comparisons between observations and simulations in the vicinity of galaxies where GSW effects originate and are strongest may provide one of the most useful ways to probe star formation and its all-important feedback processes.

We thank Ed Jenkins for kindly providing emission tables for the oxygen species. We thank Ed Jenkins, Jerry Ostriker, and Mike Shull for useful comments. The simulations were performed at the Pittsburgh Supercomputing Center. We thank R. Reddy at the Pittsburgh Supercomputing Center for constant and helpful assistance in the process of carrying out the simulations. This work was supported in part by grants NNG05GK10G and AST 05-07521. T. F. was supported by NASA through *Chandra* Postdoctoral Fellowship Award PF3-40030, issued by the *Chandra* X-Ray Observatory Center, which is operated by the Smithsonian Astrophysical Observatory for and on behalf of NASA under contract NAS 8-39073.

APPENDIX

EQUATIONS FOR NONEQUILIBRIUM EVOLUTION OF OXYGEN SPECIES

The ionization fractions of major oxygen species are calculated in a nonequilibrium evolution fashion. Specifically, we calculate the ionization fractions from O v to O ix by considering three major processes: (1) photoionization, (2) collisional ionization, and (3) recombination. If we define the ionization fraction of species i as X_i, then the time-depended evolution of X_i is determined by

$$\frac{dX_i}{dt} = -X_i\Gamma_i - \alpha_i X_i n_e - \beta_i X_i n_e + X_{i-1}\Gamma_{i-1} + \alpha_{i+1}X_{i+1}n_e + \beta_{i-1}X_{i-1}n_e. \tag{A1}$$

Here Γ is the photoionization rate of each species, given by

$$\Gamma = \int_{\nu_0}^{\infty} \frac{4\pi J_\nu}{h\nu}\sigma(\nu)d\nu, \tag{A2}$$

where ν_0 is the ionization frequency, J_ν is the background radiation, and σ is the photoionization cross section, which we adopted from Verner et al. (1996); n_e is the electron density, α is the recombination rate, adopted from Shull & Van Steenberg (1982), and β is the collisional ionization rate, adopted from Voronov (1997). We solve the combined set of equations for species O i to O iv using a first-order implicit scheme, necessary for the stiff equations considered here. Given a time step of Δt, the ion number densities at step $N+1$ are determined by the following set of equations:

$$\begin{aligned}
n_{\rm O\,V}^{N+1} &= n_{\rm O\,V}^{N} - (n_{\rm O\,V}^{N+1}n_e^N\beta_{\rm O\,V} + n_{\rm O\,V}^{N+1}\Gamma_{\rm O\,V})\Delta t + n_{\rm O\,VI}^{N+1}n_e^N\alpha_{\rm O\,V}\Delta t,\\
n_{\rm O\,VI}^{N+1} &= n_{\rm O\,VI}^{N} - (n_{\rm O\,VI}^{N+1}n_e^N\beta_{\rm O\,VI} + n_{\rm O\,VI}^{N+1}n_e^N\alpha_{\rm O\,V} + n_{\rm O\,VI}^{N+1}\Gamma_{\rm O\,VI})\Delta t\\
&\quad + (n_{\rm O\,V}^{N+1}n_e^N\beta_{\rm O\,V} + n_{\rm O\,VII}^{N+1}n_e^N\alpha_{\rm O\,V} + n_{\rm O\,V}^{N+1}\Gamma_{\rm O\,V})\Delta t,\\
n_{\rm O\,VII}^{N+1} &= n_{\rm O\,VII}^{N} - (n_{\rm O\,VII}^{N+1}n_e^N\beta_{\rm O\,VII} + n_{\rm O\,VII}^{N+1}n_e^N\alpha_{\rm O\,VI} + n_{\rm O\,VII}^{N+1}\Gamma_{\rm O\,VII})\Delta t\\
&\quad + (n_{\rm O\,VI}^{N+1}n_e^N\beta_{\rm O\,VI} + n_{\rm O\,VIII}^{N+1}n_e^N\alpha_{\rm O\,VI} + n_{\rm O\,VI}^{N+1}\Gamma_{\rm O\,VI})\Delta t,\\
n_{\rm O\,VIII}^{N+1} &= n_{\rm O\,VIII}^{N} - (n_{\rm O\,VIII}^{N+1}n_e^N\beta_{\rm O\,VIII} + n_{\rm O\,VIII}^{N+1}n_e^N\alpha_{\rm O\,VII} + n_{\rm O\,VIII}^{N+1}\Gamma_{\rm O\,VIII})\Delta t\\
&\quad + (n_{\rm O\,VII}^{N+1}n_e^N\beta_{\rm O\,VII} + n_{\rm O\,IX}^{N+1}n_e^N\alpha_{\rm O\,VII} + n_{\rm O\,VII}^{N+1}\Gamma_{\rm O\,VII})\Delta t.
\end{aligned} \tag{A3}$$

This set of equations is completed by

$$n_{\rm O\,IX} = n_{\rm O} - (n_{\rm O\,V} + n_{\rm O\,VI} + n_{\rm O\,VII} + n_{\rm O\,VIII}). \tag{A4}$$

To simplify the notation, we define

$$x \equiv n_{\rm O\,V}, \qquad y \equiv n_{\rm O\,VI}, \qquad z \equiv n_{\rm O\,VII}, \qquad w \equiv n_{\rm O\,VIII}; \tag{A5}$$

the final solution to equation (A3) is then

$$\begin{aligned}
x^{N+1} &= b^7x^N + b^8y^N + b^9z^N + b^{10}w^N + b^{10}a^{11}n_{\rm O},\\
y^{N+1} &= \left(b^1b^7 - \frac{1}{a^2}\right) + b^1b^8y^N + b^1b^9z^N + b^1b^{10}w^N + b^1b^{10}a^{11}n_{\rm O},\\
z^{N+1} &= (b^2b^7 - b^3) + \left(b^2b^8 - \frac{1}{a^5}\right)y^N + b^2b^9z^N + b^2b^{10}w^N + b^2b^{10}a^{11}n_{\rm O},\\
w^{N+1} &= (b^4b^7 + b^5) + (b^4b^8 - b^6)y^N + \left(b^4b^9 - \frac{1}{a^8}\right)z^N + b^4b^{10}w^N + b^4b^{10}a^{11}n_{\rm O}.
\end{aligned} \tag{A6}$$

Here we have defined

$$\begin{aligned}
&a^1 \equiv n_e^N\beta_{\rm O\,V}\Delta t, \qquad a^2 \equiv n_e^N\alpha_{\rm O\,V}\Delta t, \qquad a^3 \equiv \Gamma_{\rm O\,V}\Delta t, \qquad a^4 \equiv n_e^N\beta_{\rm O\,VI}\Delta t,\\
&a^5 \equiv n_e^N\alpha_{\rm O\,VI}\Delta t, \qquad a^6 \equiv \Gamma_{\rm O\,VI}\Delta t, \qquad a^7 \equiv n_e^N\beta_{\rm O\,VII}\Delta t, \qquad a^8 \equiv n_e^N\alpha_{\rm O\,VII}\Delta t,\\
&a^9 \equiv \Gamma_{\rm O\,VII}\Delta t, \qquad a^{10} \equiv n_e^N\beta_{\rm O\,VIII}\Delta t, \qquad a^{11} \equiv n_e^N\alpha_{\rm O\,VIII}\Delta t, \qquad a^{12} \equiv \Gamma_{\rm O\,VIII}\Delta t
\end{aligned} \tag{A7}$$

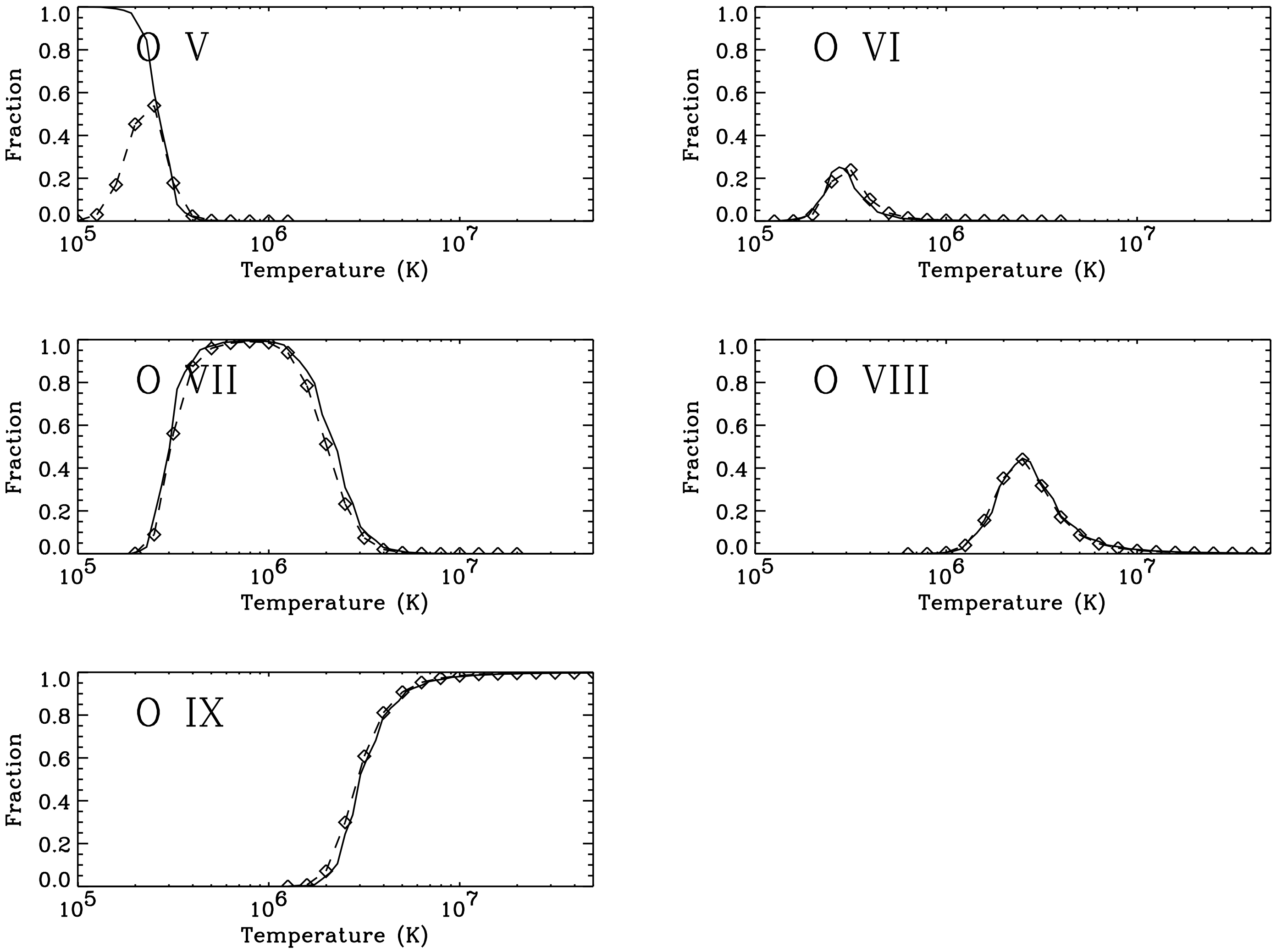

Fig. 25.—Comparison between our calculation with a very long integration time and an equilibrium calculation for the collisional ionization case with zero background radiation field. The solid curve in each panel is the result from our calculation, and the diamonds are adopted from Mazzotta et al. (1998), based on collisional ionization equilibrium.

and

$$\begin{aligned}
b^1 &\equiv (1 + a^1 + a^3)(a^2)^{-1},\\
b^2 &\equiv [(1 + a^1 + a^3)(1 + a^2 + a^4 + a^6) - (a^1 + a^3)a^2](a^2a^5)^{-1},\\
b^3 &\equiv (1 + a^2 + a^4 + a^6)(a^2a^5)^{-1},\\
b^4 &\equiv [(1 + a^5 + a^7 + a^9)b^2 - (a^4 + a^6)b^1](a^8)^{-1},\\
b^5 &\equiv [(a^4 + a^6) - (1 + a^5 + a^7 + a^9)a^2b^3](a^2a^8)^{-1},\\
b^6 &\equiv (1 + a^5 + a^7 + a^9)(a^5a^8),\\
b^7 &\equiv [a^{11}/a^2 - (a^7 + a^9 - a^{11})b^3 - (1 + a^8 + a^{10} + a^{11} + a^{12})b^5]\\
&\quad\times [(1 + a^8 + a^{10} + a^{11} + a^{12})b^4 + a^{11} + a^{11}b^1 - (a^7 + a^9 - a^{11})b^2]^{-1},\\
b^8 &\equiv [(1 + a^8 + a^{10} + a^{11} + a^{12})b^6 - (a^7 + a^9 - a^{11})/a^5]\\
&\quad\times [(1 + a^8 + a^{10} + a^{11} + a^{12})b^4 + a^{11} + a^{11}b^1 - (a^7 + a^9 - a^{11})b^2]^{-1},\\
b^9 &\equiv [(1 + a^8 + a^{10} + a^{11} + a^{12})/a^8]\\
&\quad\times [(1 + a^8 + a^{10} + a^{11} + a^{12})b^4 + a^{11} + a^{11}b^1 - (a^7 + a^9 - a^{11})b^2]^{-1},\\
b^{10} &\equiv [(1 + a^8 + a^{10} + a^{11} + a^{12})b^4 + a^{11} + a^{11}b^1 - (a^7 + a^9 - a^{11})b^2]^{-1}.
\end{aligned} \tag{A8}$$

We test our equations by comparing calculations against ionization fractions obtained from various literature sources and/or output from Cloudy (Ferland et al. 1998), based on three cases: (1) collisional ionization only, (2) including additional photoionization with a

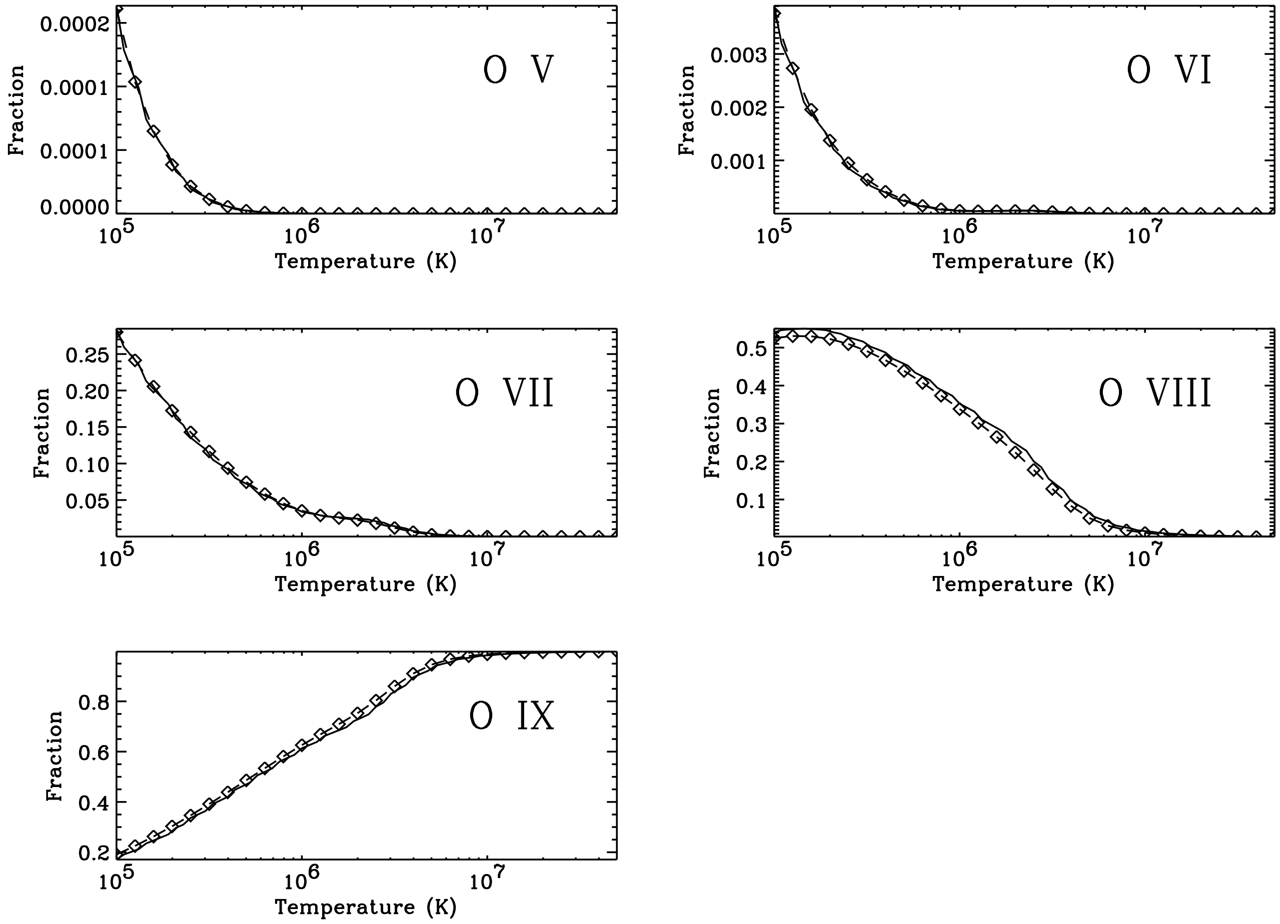

FIG. 26.—Same as Fig. 25, with the addition of a background radiation field of $J(912\ \text{Å}) = 10^{-22}$ ergs s^{-1} cm^{-2} Hz^{-1} sr^{-1}.

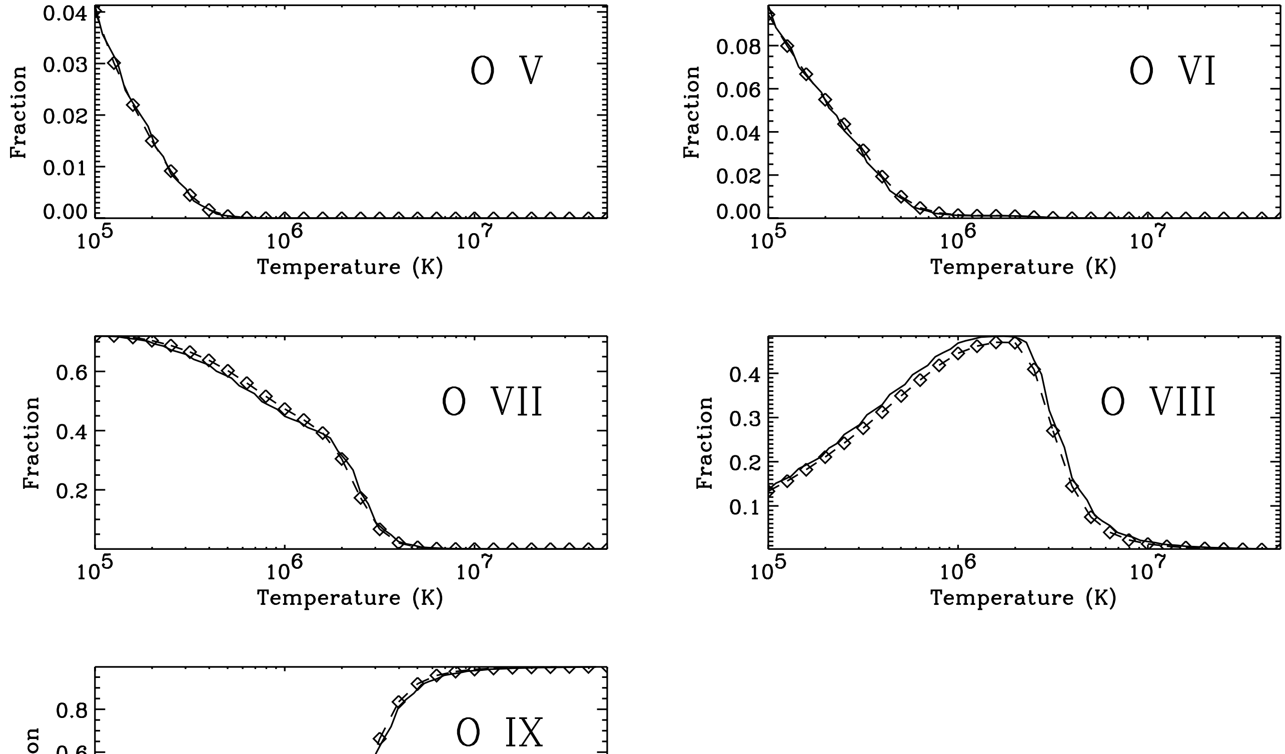

FIG. 27.—Same as Fig. 25, with a different background radiation field of $J(912\ \text{Å}) = 10^{-23}$ ergs s^{-1} cm^{-2} Hz^{-1} sr^{-1}.

background radiation field of $J(912\ \text{Å}) = 10^{-22}$ ergs s^{-1} cm^{-2} Hz^{-1} sr^{-1}, and (3) photoionization with a background radiation field of $J(912\ \text{Å}) = 10^{-23}$ ergs s^{-1} cm^{-2} Hz^{-1} sr^{-1}. Here $J(912\ \text{Å})$ is the specific flux at 912 Å, and we adopt a power-law spectrum with a spectral index of -1. To make comparisons with available equilibrium calculations, we run our simulations long enough so that eventually all the ion species are in ionization equilibrium. Figure 25 shows the comparison for the collisional ionization case with zero background radiation field. The solid curve in each panel is the result from our calculation, and the diamonds are adopted from Mazzotta et al. (1998). Except for O v, all the ion species show excellent agreement between our calculations and those from Mazzotta et al., which were calculated based on collisional ionization equilibrium. Figures 26 and 27 show the comparisons for cases 2 and 3, respectively. The symbols are the same as in Figure 25. These comparisons clearly demonstrate that our simulation reproduces the ionization fractions under a variety of possible cases that have bearing on our actual calculations.

REFERENCES

Aldrovandi, S. M. V., & Péquignot, D. 1973, A&A, 25, 137 (erratum 47, 321 [1976])
Allende Prieto, C., Lambert, D. L., & Asplund, M. 2001, ApJ, 556, L63
Arnaud, M., & Raymond, J. 1992, ApJ, 398, 394
Arnaud, M., & Rothenflug, R. 1985, A&AS, 60, 425
Arnett, D. 1996, Supernovae and Nucleosynthesis (Princeton: Princeton Univ. Press)
Asplund, M., Grevesse, N., Sauval, A. J., Allende Prieto, C., & Kiselman, D. 2004, A&A, 417, 751
Baumgartner, W. H., Loewenstein, M., Horner, D. J., & Mushotzky, R. F. 2005, ApJ, 620, 680
Bolton, J. S., Haehnelt, M. G., Viel, M., & Springel, V. 2005, MNRAS, 357, 1178
Cen, R., & Ostriker, J. P. 1999, ApJ, 519, L109
———. 2006, ApJ, 649, 560
Cen, R., Tripp, T. M., Ostriker, J. P., & Jenkins, E. B. 2001, ApJ, 559, L5
Chen, X., Weinberg, D. H., Katz, N., & Davé, R. 2003, ApJ, 594, 42
Clark, R. E. H., Cowan, R. D., & Bobrowicz, F. W. 1986, At. Data Nucl. Data Tables, 34, 415
Danforth, C. W., & Shull, J. M. 2005, ApJ, 624, 555
Davé, R., et al. 2001, ApJ, 552, 473
Dupke, R. A., & White, R. E., III. 2000, ApJ, 537, 123
Ettori, S. 2005, MNRAS, 362, 110
Fang, T., & Bryan, G. L. 2001, ApJ, 561, L31
Fang, T., Bryan, G. L., & Canizares, C. R. 2002a, ApJ, 564, 604
Fang, T., Croft, R. A. C., Sanders, W. T., Houck, J., Davé, R., Katz, N., Weinberg, D. H., & Hernquist, L. 2005, ApJ, 623, 612
Fang, T., Marshall, H. L., Lee, J. C., Davis, D. S., & Canizares, C. R. 2002b, ApJ, 572, L127
Ferland, G. J., Korista, K. T., Verner, D. A., Ferguson, J. W., Kingdon, J. B., & Verner, E. M. 1998, PASP, 110, 761
Finoguenov, A., Briel, U. G., & Henry, J. P. 2003, A&A, 410, 777
Furlanetto, S. R., Phillips, L. A., & Kamionkowski, M. 2005a, MNRAS, 359, 295
Furlanetto, S. R., Schaye, J., Springel, V., & Hernquist, L. 2004, ApJ, 606, 221
———. 2005b, ApJ, 622, 7
Haardt, F., & Madau, P. 1996, ApJ, 461, 20
Kaastra, J. S., Lieu, R., Tamura, T., Paerels, F. B. S., & den Herder, J. W. 2003, A&A, 397, 445
Mathur, S., Weinberg, D. H., & Chen, X. 2003, ApJ, 582, 82
Mazzotta, P., Mazzitelli, G., Colafrancesco, S., & Vittorio, N. 1998, A&AS, 133, 403
Mushotzky, R. F., Loewenstein, M., Arnaud, K. A., Tamura, T., Fukazawa, Y., Matsushita, K., Kikuchi, K., & Hatsukade, I. 1996, ApJ, 466, 686
Nicastro, F., et al. 2002, ApJ, 573, 157
———. 2005, Nature, 433, 495
Oegerle, W. R., et al. 2000, ApJ, 538, L23
Ohashi, T., et al. 2006, Adv. Space Res., in press (Proc. 35th COSPAR Sci. Assem., No. 3772)
Pettini, M., Rix, S. A., Steidel, C. C., Adelberger, K. L., Hunt, M. P., & Shapley, A. E. 2002, ApJ, 569, 742
Portinari, L., Moretti, A., Chiosi, C., & Sommer-Larsen, J. 2004, ApJ, 604, 579
Rauch, M., et al. 1997, ApJ, 489, 7
Savage, B. D., Sembach, K. R., Tripp, T. M., & Richter, P. 2002, ApJ, 564, 631
Scharf, C., Donahue, M., Voit, G. M., Rosati, P., & Postman, M. 2000, ApJ, 528, L73
Sembach, K. R., Tripp, T. M., Savage, B. D., & Richter, P. 2004, ApJS, 155, 351
Shull, J. M., Roberts, D., Giroux, M. L., Penton, S. V., & Fardal, M. A. 1999, AJ, 118, 1450
Shull, J. M., Tumlinson, J., & Giroux, M. L. 2003, ApJ, 594, L107
Shull, J. M., & Van Steenberg, M. 1982, ApJS, 48, 95 (erratum 49, 351)
Spergel, D. N., et al. 2003, ApJS, 148, 1
Suto, Y., et al. 2004, J. Korean Astron. Soc., 37, 387
Tamura, T., Kaastra, J. S., den Herder, J. W. A., Bleeker, J. A. M., & Peterson, J. R. 2004, A&A, 420, 135
Tegmark, M., et al. 2004, Phys. Rev. D, 69, No. 103501
Tittley, E. R., & Henriksen, M. 2001, ApJ, 563, 673
Tripp, T. M., & Savage, B. D. 2000, ApJ, 542, 42
Tripp, T. M., Savage, B. D., & Jenkins, E. B. 2000, ApJ, 534, L1
Tsujimoto, T., Nomoto, K., Yoshii, Y., Hashimoto, M., Yanagida, S., & Thielemann, F.-K. 1995, MNRAS, 277, 945
Verner, D. A., & Ferland, G. J. 1996, ApJS, 103, 467
Verner, D. A., Ferland, G. J., Korista, K. T., & Yakovlev, D. G. 1996, ApJ, 465, 487
Voronov, G. S. 1997, At. Data Nucl. Data Tables, 65, 1
Yoshikawa, K., Yamasaki, N. Y., Suto, Y., Ohashi, T., Mitsuda, K., Tawara, Y., & Furuzawa, A. 2003, PASJ, 55, 879
Yoshikawa, K., et al. 2004, PASJ, 56, 939